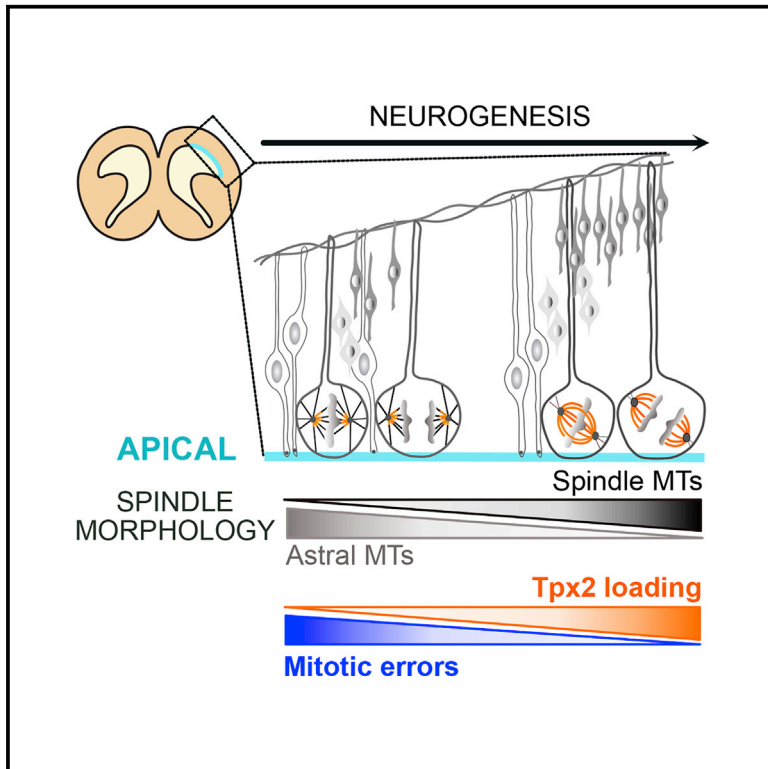


# Current Biology

## Differences in Mitotic Spindle Architecture in Mammalian Neural Stem Cells Influence Mitotic Accuracy during Brain Development

### Graphical Abstract



### Authors

Diana Vargas-Hurtado,  
Jean-Baptiste Brault, Tristan Piolot, ...,  
Alexandre Baffet,  
Véronique Marthiens, Renata Basto

### Correspondence

veronique.marthiens@curie.fr (V.M.),  
renata.basto@curie.fr (R.B.)

### In Brief

Vargas-Hurtado et al. report spindle morphology tailoring during brain development and identify TPX2 as a main contributor. They show that changes in spindle architecture are translated into different susceptibility to mitotic errors. They propose that tuning of spindle organization influences the response of mitotic stem cells to adverse situations.

### Highlights

- Mitotic spindle architecture changes during mammalian neurogenesis
- Early-stage spindles contain more astral MTs and less spindle MTs
- TPX2 loading on spindle microtubules influences spindle morphology
- Spindles are more prone to chromosome segregation errors during early neurogenesis

# Differences in Mitotic Spindle Architecture in Mammalian Neural Stem Cells Influence Mitotic Accuracy during Brain Development

Diana Vargas-Hurtado,<sup>1</sup> Jean-Baptiste Brault,<sup>2</sup> Tristan Piolot,<sup>3</sup> Ludovic Leconte,<sup>4</sup> Nathalie Da Silva,<sup>1</sup> Carole Pennetier,<sup>1</sup> Alexandre Baffet,<sup>2</sup> Véronique Marthiens,<sup>1,\*</sup> and Renata Basto<sup>1,5,\*</sup>

<sup>1</sup>Biology of Centrosomes and Genetic Instability Team, Curie Institute, PSL Research University, CNRS, UMR144, 12 rue Lhomond, Paris 75005, France

<sup>2</sup>Cell Biology of Mammalian Neurogenesis, Curie Institute, PSL Research University, CNRS, UMR144, 12 rue Lhomond, Paris 75005, France

<sup>3</sup>Cell and Tissue Imaging Facility (PICT-IBiSA), Curie Institute, CNRS, U934/UMR 3215, rue Pierre et Marie Curie, Paris 75005, France

<sup>4</sup>Cell and Tissue Imaging Facility (PICT-IBiSA), Curie Institute, CNRS, UMR 144, 12 rue Lhomond, Paris 75005, France

<sup>5</sup>Lead Contact

\*Correspondence: [veronique.marthiens@curie.fr](mailto:veronique.marthiens@curie.fr) (V.M.), [renata.basto@curie.fr](mailto:renata.basto@curie.fr) (R.B.)

<https://doi.org/10.1016/j.cub.2019.07.061>

## SUMMARY

A functional bipolar spindle is essential to segregate chromosomes correctly during mitosis. Across organisms and cell types, spindle architecture should be optimized to promote error-free divisions. However, it remains to be investigated whether mitotic spindle morphology adapts to changes in tissue properties, typical of embryonic development, in order to ensure different tasks, such as spindle positioning and chromosome segregation. We have characterized mitotic spindles in neural stem cells (NSCs) of the embryonic developing mouse neocortex. Surprisingly, we found a switch in spindle morphology from early to late neurogenic stages, which relies on an increase in inner spindle microtubule density and stability. Mechanistically, we identified the microtubule-associated protein TPX2 as one determinant of spindle shape, contributing not only to its robustness but also to correct chromosome segregation upon mitotic challenge. Our findings highlight a possible causal relationship between spindle architecture and mitotic accuracy with likely implications in brain size regulation.

## INTRODUCTION

Accurate chromosome segregation depends on the assembly of a bipolar spindle that connects sister chromatids to each spindle pole [1]. Spindle bipolarity is a conserved feature of mitotic cells, even if variations in spindle morphology and size have been widely observed among different cell types and organisms [1–4]. Whether cells can adapt spindle morphology according to changes in tissue environment during development is not known.

During mammalian brain development, neural stem cells (NSCs) undergo a concerted number of divisions before giving rise to neurons and glial cells [5]. Their number is tightly regulated and ultimately determines brain size and function [6]. Primary recessive

microcephaly (MCPH) is characterized by brain size reduction at birth [7]. MCPH mutations were identified in genes encoding for centrosome or spindle components, indicating that brain development is particularly vulnerable to these mutations [8–10]. Microcephaly models in *Drosophila* [11, 12], mouse [13–16], and ferret [17] revealed that small brains result from a decrease in the NSC population. Mis-position away from the ventricle, cell-cycle arrest, mitotic delay, or chromosome mis-segregation can lead to reduction of the NSC pool by triggering cell death and/or premature neuronal differentiation [13–16, 18–20].

During neurogenesis, NSCs switch from proliferative symmetric divisions (responsible for expanding the NSC pool) to asymmetric neurogenic divisions, which give rise to committed neuronal precursors [21]. Mitotic spindles have to be positioned according to the mode of division through astral MT interactions with a polarized cell cortex [22, 23]. It remains to be determined whether other spindle functions are impacted during neurogenesis.

## RESULTS

### Spindle Morphology Changes during Neurogenesis

We analyzed mitotic spindle morphology during neurogenesis using the “*en face* view” protocol [24] for visualization of mitotic NSCs in the ventricular zone (VZ) [21] (Figure 1A). Brain explants were labeled with centrosomes and  $\alpha$ -tubulin antibodies to label the spindle poles and the mitotic spindle, respectively. Metaphase spindles (recognized by the alignment of all chromosomes within a cell) displayed striking differences in their architecture from early to late neurogenic stages (Figures 1B and S1A). At early neurogenic stages, from embryonic day 11.5 (E11.5) to E13.5, spindles displayed long astral microtubules (MTs) that contacted the cell membrane, and MT density near the chromosomes appeared low. At late neurogenic stages (from E16.5 onward), fewer and shorter astral MTs were detected, and MT density within the inner spindle was increased. Importantly, these changes in spindle morphology were observed in the same population of NSCs that express the transcription factor Pax6 (Figure S1C) [21].

To quantitatively evaluate spindle morphology differences, we plotted tubulin fluorescence intensity (FI) profiles that span from

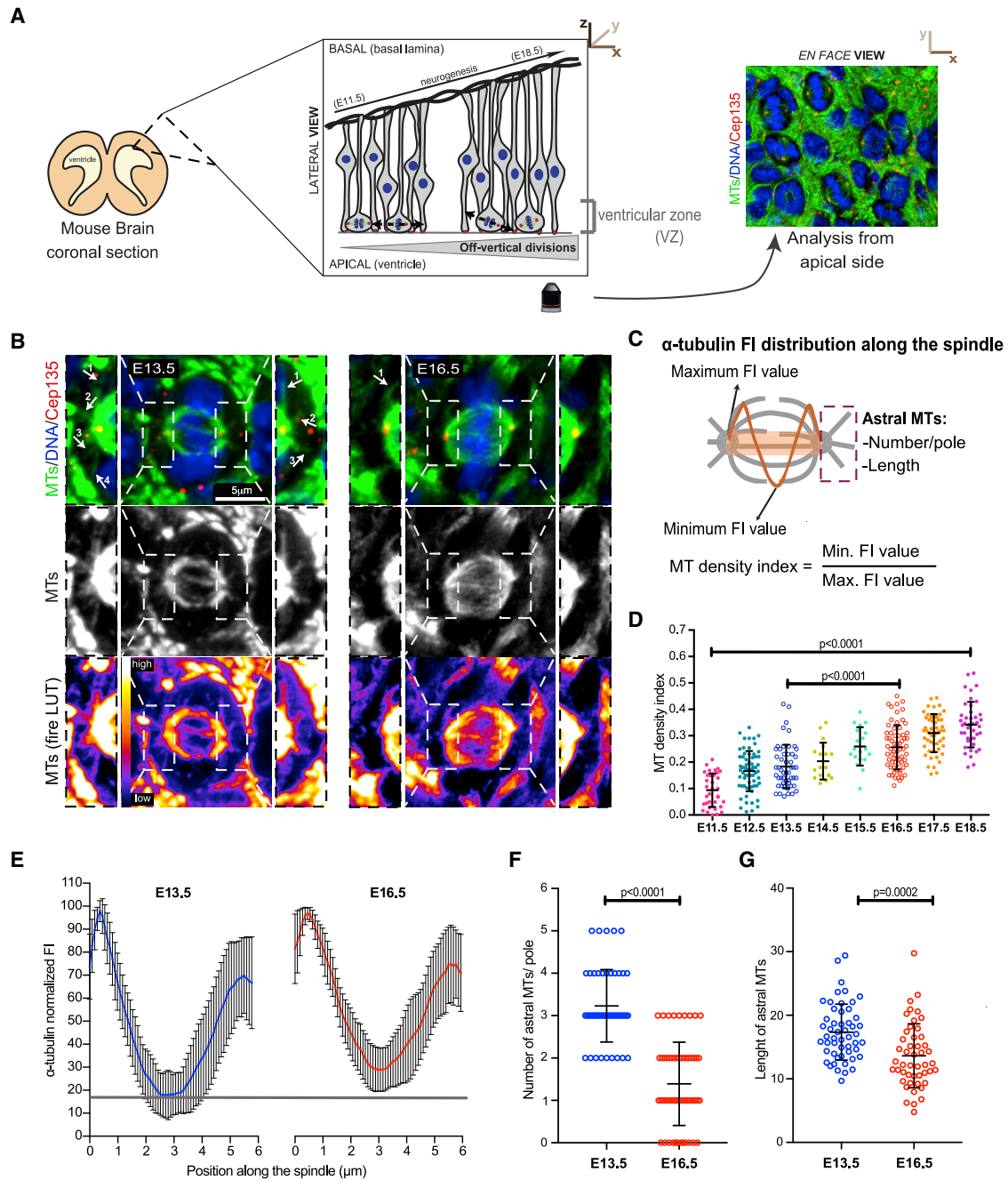


**Figure 1. NSC Spindle Architecture Variations during Neurogenesis**

(A) Left: diagram depicting the organization of NSCs in the developing mouse neocortex during neurogenesis. Right: *en face* view confocal acquisition of mitotic NSCs is shown.

(B) Representative confocal images of metaphase spindles at E13.5 and E16.5. Left and right insets: magnifications of astral MTs at each spindle pole are shown (arrows).

(C) Procedure to evaluate astral MTs and inner spindle MT density index (STAR Methods).

(D) Dot plot graph of MT density index values at all neurogenic stages; each dot represents one cell. Error bars represent means  $\pm$  SD from at least 17 NSCs out of 4 brains per stage.

(E) Normalized  $\alpha$ -tubulin FI profiles from pole to pole in E13.5 (blue line,  $n = 53$ ) and E16.5 (red line,  $n = 47$ ) spindles. Each data point represents the mean value  $\pm$  SD at a given position along the spindle.

(F and G) Dot plot graphs indicating the number (F) and length (G) of astral MTs per spindle pole in E13.5 (blue) and E16.5 (red) NSCs. In (F), each dot corresponds to one spindle (E13.5,  $n = 52$ ; E16.5,  $n = 59$ ) and in (G) to one individual astral MT (E13.5,  $n = 52$ ; E16.5,  $n = 48$ ). Error bars represent means  $\pm$  SD from at least 26 NSCs. Unpaired *t* tests were used for statistics.

Scale bar, 5  $\mu\text{m}$  (B). See also [Figure S1](#).

one spindle pole to the other (Figures 1C, 1E, and S1B). By dividing the minimum FI value (at the center of the spindle) by the maximum FI value (at the spindle poles), we obtained a MT density index (Figure 1C). MT density indices increased stepwise (Figure 1D), indicating enrichment of MT bundles within the spindle inner mass during neurogenesis.

We next focused on E13.5 and E16.5 neurogenic stages because all mitotic spindles within each stage displayed the typical architecture shown in Figure 1B and because FI values and MT density index differences were highly significant between these two stages (Figures 1D and 1E). Differences in spindle length or width between both stages were not observed (Figures S1D–S1F).

Increased inner MT density in E16.5 spindles inversely correlated with the abundance of astral MTs, which were also shorter (Figures 1B, 1F, and 1G). Such a decline in the population of astral MTs has been previously correlated to the switch from vertical to off-vertical divisions that occurs in the NSC population during neurogenesis (Figure 1A) [23]. Our findings now show that both astral and spindle MT populations change in mitotic NSCs during neuro-development.

We will refer to spindles with robust astral MT arrays and low inner MT density as early or E13.5 spindles, and spindles with low astral MT numbers and higher inner MT density will be E16.5 or late spindles.

### Increase in Spindle MT Density and Stability during Neurogenesis

MT organization, nucleation, and stability influence spindle architecture [2]. To further characterize spindle architecture, we performed 3D structural illumination microscopy (3D-SIM) followed by 3D tracking and reconstruction of MT bundles (Figure 2A). We found more and longer MT bundles at E16.5 as compared to E13.5 (Figures 2B and 2C). Because spindle length was not changed (Figure S1E), we reasoned that the increase in E16.5 bundle length reflected their higher curvature (Figures 2A and 2C). Moreover, bundle width increased in E16.5 spindles (Figure 2D), suggesting that, at this stage, bundles contain more MTs.

Because E16.5 spindles displayed a higher MT density index and thicker bundles, we ascertained whether this impacted spindle stability. We depolymerized MTs with cold and compared tubulin FI values at different time points (Figure 2E). After 3 min, E13.5 spindles showed low FI values, and E16.5 spindles still contained thick bundles (Figure 2F). After 7 min, higher mean tubulin FI was observed in E16.5 spindles when compared to E13.5 (Figure 2G), indicating that MT bundles are more stable in E16.5 spindles. Because tubulin post-translational modifications (PTMs) can impact MT stability [25], we evaluated eventual differences in E13.5 and E16.5 spindle PTMs. Comparative analysis of tubulin acetylation and tyrosination did not show significant differences between the two stages (Figures S2A–S2D).

To test whether differences in MT-nucleating pathways could contribute to differences in spindle morphology, we identified the sites of MT nucleation. Cells were subjected to cold, followed by MT repolymerization at 37°C (Figure 2H). After 2 min, MTs nucleated from the centrosome at both stages, albeit E16.5 centrosomes appeared as stronger nucleators (Figure 2I). We did not observe any MT nucleation away from the centrosomes

(cytoplasmic nucleation), as observed in RPE-1 spindles used as positive control (Figures S2E and S2F). Centrosomes were the main MT-nucleating sites in NSCs at both neurogenic stages.

As E16.5 centrosomes appeared as stronger nucleators (Figures 2I and S2E), we used high-resolution microscopy to characterize the recruitment and spatial organization of centrosomal proteins in NSCs (Figures S2G and S2H). We did not detect any difference regarding protein level or organization when analyzing the main MT nucleator  $\gamma$ -tubulin or other pericentriolar material (PCM) proteins Cep192 and Cdk5Rap2 (Figures S2I–S2L). Nevertheless, we observed thicker bundles nucleated from E16.5 centrosomes after MT repolymerization assays (Figures 2I and 2J). Altogether, E16.5 spindles appeared more stable than E13.5 spindles.

### Identification of Spindle Morphology Determinants

Because we excluded the involvement of tubulin PTMs and centrosome activity in spindle morphogenesis alterations (Figures S2A–S2D and S2G–S2L), we postulated that changes in the landscape of microtubule-associated proteins (MAPs), which can tune spindle morphology, may contribute to the differences described above [2]. We evaluated the levels and distribution of MAPs with important roles in bipolar spindle assembly. We used antibodies against HSET, Eg5, TPX2, and the motor protein CENP-E. Of these, CENP-E and HSET did present similar distributions at both stages (Figures S3A–S3E).

We then analyzed the MT stabilizing, nucleating, and bundling factor TPX2 [26–28], which contributes to morphology changes in the meiotic spindles of *Xenopus* species [29], and the motor protein Eg5 [30]. We observed similar changes in the distribution of these proteins when comparing E13.5 and E16.5 spindles. At E13.5, they were associated with MT minus ends and particularly enriched near the poles, and at E16.5, they were distributed all along the MTs (Figures 3A and S3F). Accordingly, evaluation of their distribution along the spindles and of density index values confirmed their accumulation near the chromosomes at E16.5, even if more pronounced in the case of TPX2 (Figures 3B, 3C, S3G, and S3H).

Because the pool of TPX2s associated with spindle MTs appeared higher at E16.5, we tested whether it reflected an overall increase in cytoplasmic TPX2 levels. We isolated NSCs by fluorescent-activated cell sorting (FACS) and analyzed total TPX2 levels by western blot. TPX2 levels were similar at both stages (Figures 3D and 3E), despite a slight increase in  $\alpha$ -tubulin levels at E16.5 (Figure 3F). These results suggested that TPX2 loading was increased on spindle MTs from E13.5 to E16.5, and total protein levels remained unchanged. Altogether, Eg5 and TPX2 appeared as the most relevant candidates to explain spindle morphology changes.

### TPX2 Is One Determinant of NSC Spindle Morphology

To functionally test Eg5 involvement in spindle morphology differences, we used low doses of the monastrol inhibitor [31] to partially inhibit Eg5 protein activity without compromising spindle bipolarity in E16.5 cortical explants. We observed a reduction in E16.5 spindle length, confirming the effective action of the drug (Figures S4A and S4B). However, Eg5 inhibition did not change spindle morphology, as spindles from Ctrl and Monastrol-treated explants showed similar MT density indices (Figures

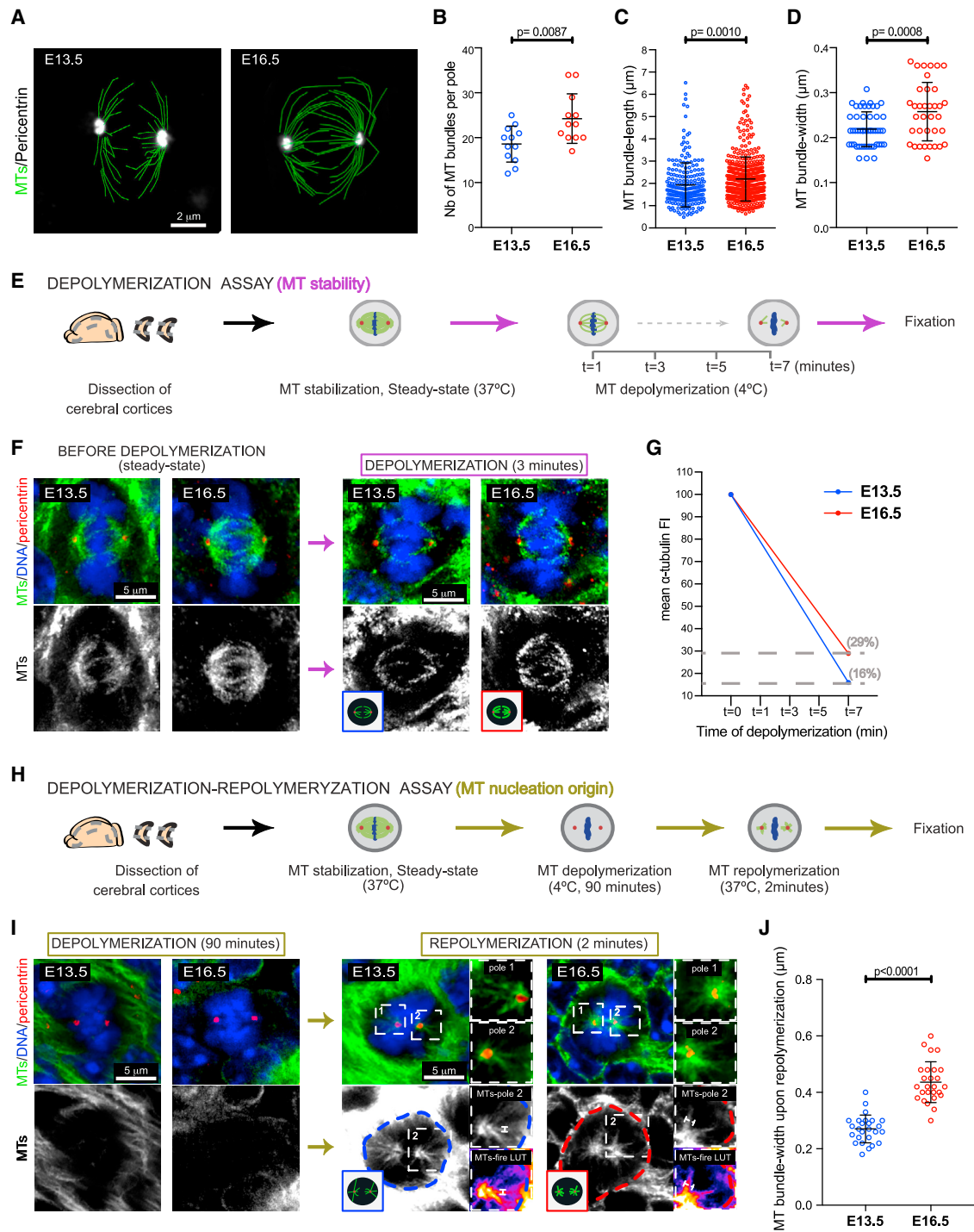


**Figure 2. E16.5 Spindles Displayed More Stable and Thicker MT Bundles**

(A) 3D reconstructions of spindles imaged with SIM in E13.5 and E16.5 cerebral cortices.

(B–D) Tracking of spindle fibers enabled to extract MT bundle density (B), length (C), and width (D). In (B), each dot represents one cell and in (C) and (D) one MT bundle (C, E13.5,  $n = 226$ , E16.5,  $n = 472$ ; D, E13.5,  $n = 51$ , E16.5,  $n = 37$ ). Error bars represent means  $\pm$  SD from at least 12 mitotic NSCs out of 4 brains.

(E) Schematic representation of MT depolymerization assays (STAR Methods).

(F) Representative images of MT bundles in E13.5 and E16.5 mitotic spindles before (left panels) and after 3 min of cold treatment (right panels).

(G) Quantifications of  $\alpha$ -tubulin mean FI along E13.5 (blue) and E16.5 (red) spindles before ( $t = 0$ ) and after 7 min of MT depolymerization ( $t = 7$ ). Mean FI at  $t = 0$  was normalized to 100% at each stage. More than 15 cells were analyzed at each time point.

(H) Schematic representation of MT depolymerization and repolymerization assays (STAR Methods).

(legend continued on next page)

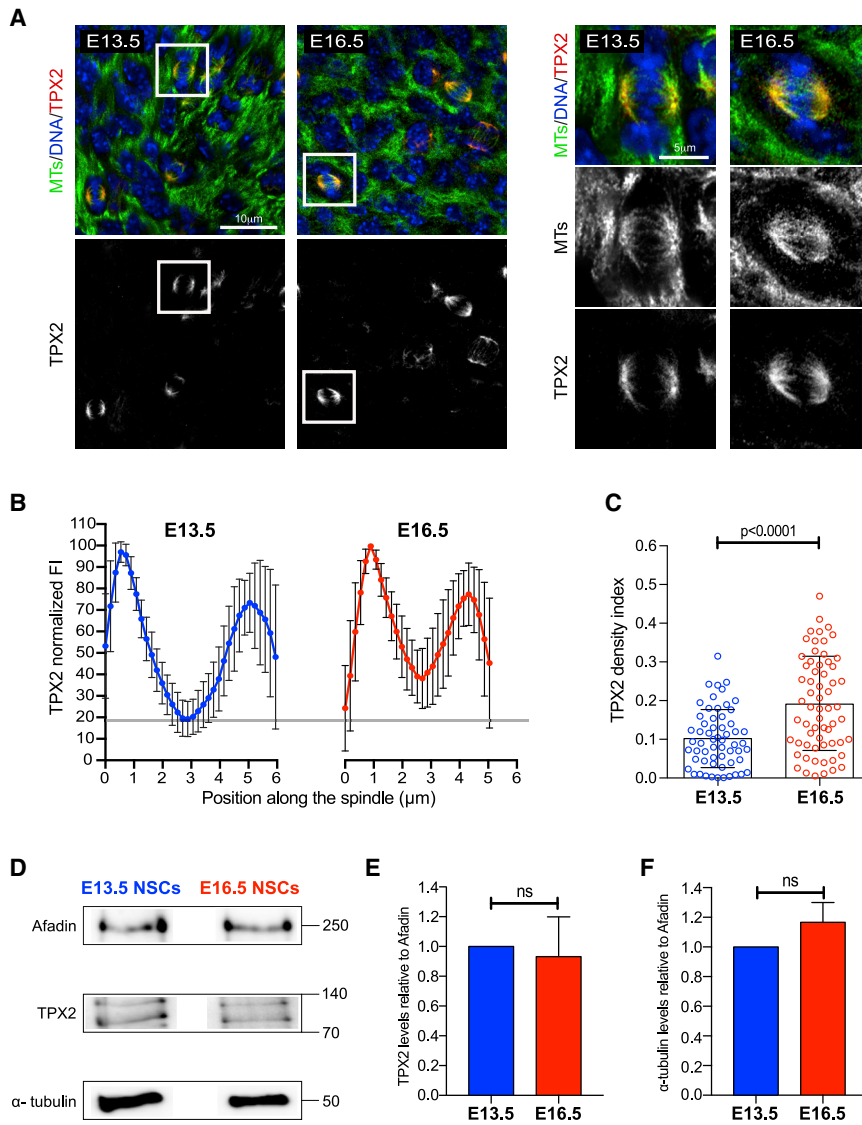


**Figure 3. Increased TPX2 Loading in E16.5 Spindles**

(A) Left: representative confocal images of E13.5 and E16.5 cortical explants. Right: magnifications of metaphase spindles are shown (white boxes in left panels).

(B) FI profiles of TPX2 distribution along E13.5 (blue,  $n = 31$ ) and E16.5 (red,  $n = 29$ ) spindles. Each data point represents the mean value  $\pm$  SD at a given position along the spindle.

(C) Dot plot graph of TPX2 density index values in E13.5 and E16.5 NSCs. Each dot represents one cell (E13.5,  $n = 59$ ; E16.5,  $n = 63$ ); error bars represent means  $\pm$  SD. Unpaired t tests were used for statistics.

(D) Western blot analysis of  $\alpha$ -tubulin (bottom) and Tpx2 (middle) total protein content in FACS-sorted NSC extracts. Afadin was used as loading control (upper lane).

(E and F) Graph bars showing total TPX2 protein (E) and  $\alpha$ -tubulin (F) levels relative to loading controls. ns, non-significant. Mann-Whitney non-parametric test was used for statistics.

Scale bars, 10  $\mu$ m (A, left) and 5  $\mu$ m (A, right). See also Figure S3.

appeared similar to E13.5 spindles, as they displayed more astral MTs (Figure 4B), reduced MT density in the inner spindle region (Figures 4B, 4D, and 4E), and decreased MT bundle width (Figure 4F). Importantly, TPX2-MT-associated FI levels directly correlated with both MT density index and spindle morphology (Figures 4G and 4H). These results identified TPX2 as one main contributor of spindle morphology switch.

A decrease in the number of astral MTs accompanies the switch from vertical to off-vertical divisions that occurs during neurogenesis (Figure 1A) [23]. We thus investigated whether changes in TPX2 levels were sufficient to alter spindle positioning in the VZ.

We observed a higher frequency of vertical divisions (parallel to the ventricular lining) in E16.5 explants electroporated with TPX2 siRNA as compared to Ctrl siRNA (Figures 4I–4K). We concluded that the spindle switch in response to TPX2 depletion also impacts spindle orientation.

To determine the relevance of TPX2 function during brain morphogenesis, we depleted TPX2 using *in utero* electroporation of E13.5 brains [34]. We analyzed the consequences on NSC division and fate in brain coronal sections 48 h later (E15.5) using brain lipid-binding protein (BLBP)-GFP expression as a positive marker of NSC transfection (Figure S4D). A high frequency of mitotic spindles with abnormal configurations (monopolar and/or low MT density) was observed, illustrating

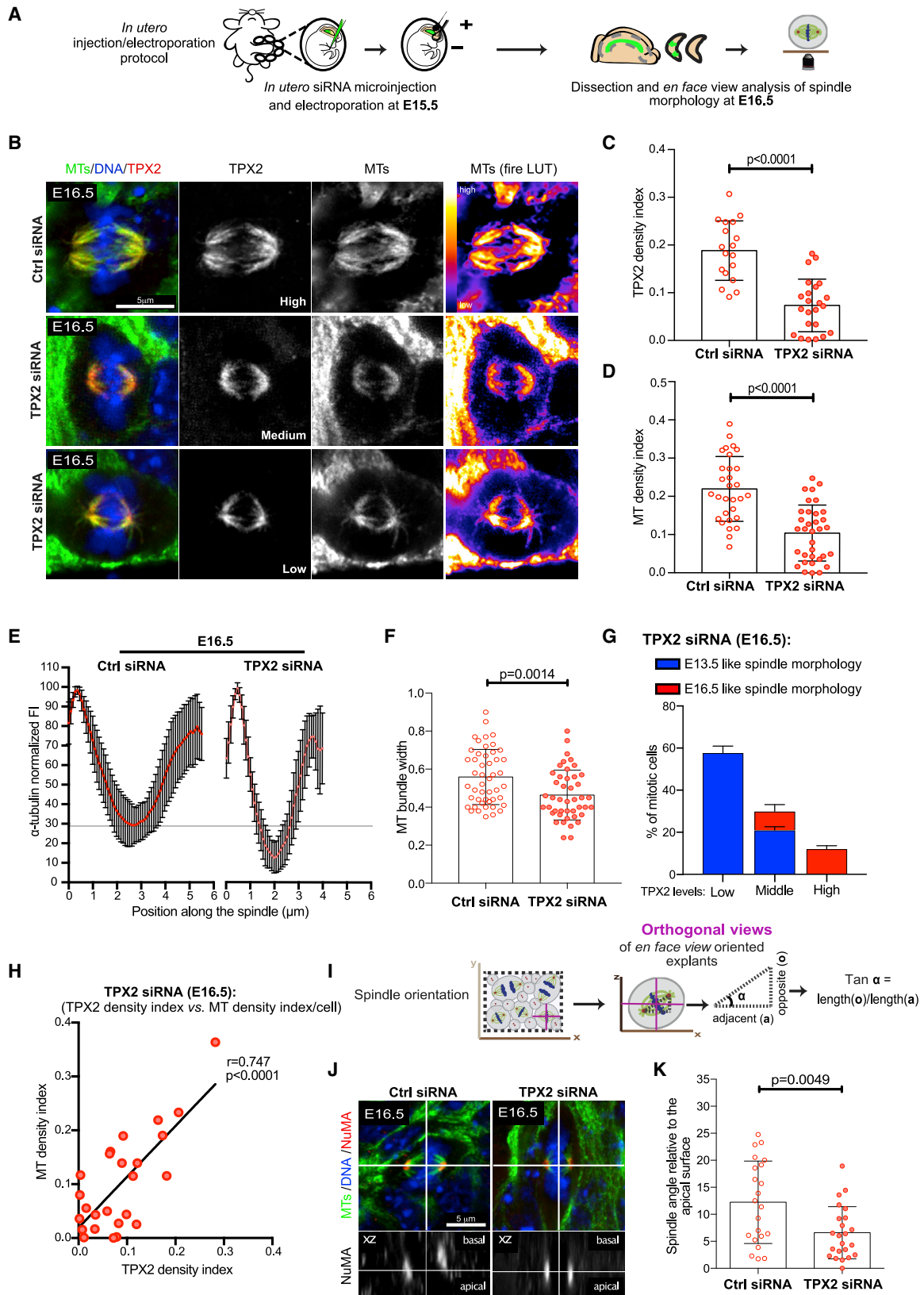
S4A–S4C). We concluded that Eg5 is not involved in shaping NSC spindle morphology.

We next investigated the contribution of TPX2. We decreased TPX2 levels by *in utero* electroporation of E15.5 brains with short interfering (si)RNAs and analyzed mitotic spindles after 24 h (E16.5; Figure 4A). We evaluated that the concentration of TPX2 siRNA to be injected into the ventricle should be of 50 nM in order to slightly decrease the levels of TPX2 (partial depletion) instead of totally depleting the protein, which would impair bipolar spindle formation [26, 32, 33]. In these conditions, we could observe a reduction in the levels of the protein loaded on spindle MTs without compromising spindle bipolarity (Figures 4B and 4C). After partial TPX2 depletion, E16.5 spindle architectures

(I) Representative images of E13.5 and E16.5 NSCs after MT depolymerization (left panels) and 2 min after repolymerization (right panels). Insets show magnifications of MTs nucleated at each spindle pole (dashed boxes).

(J) Dot plot graph depicting MT bundle widths 2 min after repolymerization. Each dot represents one MT bundle at E13.5 (blue,  $n = 26$ ) and E16.5 (red,  $n = 26$ ). Error bars represent means  $\pm$  SD from at least 9 mitotic NSCs. For (B)–(D) and (J), unpaired t tests were used for statistics.

Scale bars, 2  $\mu$ m (A) and 5  $\mu$ m (F and I). See also Figure S2.



(legend on next page)

the efficiency of TPX2 downregulation (Figures S4E and S4F). When bipolar spindles were formed, we noticed a high frequency of NSCs with misaligned chromosomes (Figures S4E and S4G), confirming the role of TPX2 in generating functional spindles in mouse NSCs. Further, although in Ctrl brains, NSCs and neurons occupy distinct layers along the apico-basal axis [21], they were intermingled in TPX2 siRNA brains (Figure S4H). Moreover, analysis of GFP-expressing cells (NSCs and their progeny) in TPX2 siRNA brains revealed an increased proportion of neurons generated at the expense of NSCs in comparison with Ctrl siRNA brains (Figure S4I). Premature neuronal differentiation leads to early depletion of the NSC pool and brain size reduction—microcephaly [11, 14, 16, 19, 20, 35].

Overall, and in agreement with a previous study [27], our results support a key role for TPX2 in the regulation of NSC division, positioning, and fate.

### Identification of TPX2 Domains Influencing Spindle Morphology

The pleiotropic roles played by TPX2 during brain morphogenesis *in vivo* prevented further analysis on the function of TPX2 in spindle assembly. We took advantage of an *in vitro* 2D culture assay that enabled the expansion of primary NSCs *in vitro* (Figure S5A). We adapted the protocol from [36], where a nearly pure population of NSCs can be obtained (Figures S5B and S5C). E16.5-derived primary NSC cultures assembled mitotic spindles similar to spindles observed *in vivo*: few astral MTs and high inner spindle MT density (Figures S5D–S5F).

TPX2 is a monomeric protein that contains multiple MT-binding regions [37, 38], one domain of interaction with the kinase Aurora-A (N-terminal region [N-TER]) [39], and one with the motor protein Eg5 (C-terminal region [C-TER]) [40]. TPX2 is also an importin  $\alpha$ -regulated cargo, which influences chromatin-mediated MT nucleation [41] (Figure 5A). We first confirmed that TPX2 is required to regulate spindle morphology in primary NSCs. As previously described [26, 43], TPX2 downregulation by siRNA (Figure 5B) led to the formation of abnormal spindles (monopolar, short bipolar, or bipolar with low MT density), and the percentage of cells with normal spindles in TPX2-depleted condition was lower than in Ctrl (Figures 5B and 5C). The full-length (FL) GFP-tagged version of human TPX2 (hTPX2) rescued

spindle morphology in TPX2-depleted cells (Figure 5C), validating the specificity of our conditions. We next identified TPX2 domains responsible for normal spindle assembly. After TPX2 siRNA, both hTPX2 N-TER and C-TER GFP-tagged versions rescued the number of spindles with normal morphology when compared to Ctrl (Figures 5A and 5C), even if higher frequency of normal spindles was observed in the TPX2 C-TER domain condition (Figure 5C). Interestingly, TPX2 loading on interphase spindle MTs was increased in hTPX2 C-TER as compared to hTPX2 N-TER transfected cells (Figure S5G).

TPX2 activity is regulated by cooperative interactions between the C-TER and N-TER regions and/or other importin  $\alpha$ -regulated factors [38, 44]. Because TPX2 N-TER region comprising the NLS sequence (Figure 5A) was only partly efficient in rescuing spindle assembly, we analyzed the contribution of importin  $\alpha$ /chromatin-mediated MT nucleation to spindle morphology. We introduced point mutations in hTPX2-NLS sequence (hTPX2-NLS\*). After TPX2 siRNA, hTPX2-NLS\* protein rescued spindle morphology to the same extent than TPX2 C-TER and FL proteins, even if the great majority of cells scored in the abnormal spindle category exhibited reduced spindle length (Figures 5B and 5C). This result suggested that, yet important for spindle length regulation, regulation of TPX2 activity by importin  $\alpha$  did not influence spindle architecture. Accordingly, we did not observe significant changes in the levels of other importin  $\alpha$ -regulated proteins like HSET (Figure S3C) or Ran guanine nucleotide exchange factor, RCC1 (Figures S5H and S5I), during neurogenesis *in vivo*.

Overall, these results indicated that different TPX2 domains are required to fulfil the pleiotropic function of TPX2 in the regulation of NSC bipolar spindle formation, size, and architecture. Additionally, they excluded the possibility that differences in activation of the Ran pathway contributed to the function of TPX2 in shaping spindle architecture. Nevertheless, they strengthened our previous observations that the extent of TPX2 loading on MTs contributes to NSC spindle architectures.

### Differences in Spindle Morphology Impact Mitotic Fidelity

We reasoned that changes in TPX2 loading status during neurogenesis might be translated into different capacity of NSCs to preserve mitotic fidelity in adverse situations. We compared

#### Figure 4. TPX2 Is Determinant in NSC Spindle Morphology and Orientation

- (A) Schematic representation of the protocol used to decrease TPX2 levels in E16.5 cortical explants *in vivo*.  
 (B) Representative confocal images of E16.5 mitotic spindles in metaphase 24 h after electroporation of Ctrl (upper panels) and TPX2 (middle and lower panels) siRNAs.  
 (C) Dot plot graph displaying TPX2 density indices in E16.5 NSCs after Ctrl (n = 18) and TPX2 (n = 23) siRNA *in utero* electroporation.  
 (D) Dot plot graph showing MT density indices in E16.5 spindles after Ctrl (n = 30) and TPX2 siRNAs (n = 34).  
 (E) Normalized FI profiles of  $\alpha$ -tubulin along E16.5 spindle axis after Ctrl (red, n = 14) and TPX2 (pink, n = 18) siRNAs. Each data point represents the mean value  $\pm$  SD at a given position along the spindle.  
 (F) Dot plot graph showing MT bundle width in E16.5 spindles after Ctrl (red, n = 48) or TPX2 (pink, n = 44) siRNAs. Each dot represents one MT bundle measure.  
 (G) Bar graph representing the proportion of cells with E13.5-like (blue, low inner spindle and high astral MT density) or E16.5-like spindle morphology (red, high inner spindle and low astral MT density) after TPX2 siRNA (see B for images). Cells were categorized according to TPX2 levels at the spindles: high (n = 14), medium (n = 7), and low (n = 3); see (B) for classification.  
 (H) XY plot and corresponding linear regression between MT density and TPX2 density indices (n = 25 mitotic NSCs). Spearman r-test was used for statistics.  
 (I) Diagram depicting the protocol used to measure spindle position relative to the ventricular lining in E16.5 siRNA-electroporated explants (STAR Methods).  
 (J) Representative images of E16.5 metaphases in brains electroporated with Ctrl (left) or Tpx2 (right) siRNAs. Bottom insets show spindle pole positions relative to the ventricular lining (apical).  
 (K) Dot plot graph showing spindle angle values in E16.5 NSCs after Ctrl (left, n = 22) or Tpx2 (right, n = 23) siRNAs. Error bars represent means  $\pm$  SD from more than 3 brains and 3 replicates.  
 For (C), (D), (F), and (K), error bars represent means  $\pm$  SD and unpaired t tests were used for statistics. Scale bars, 5  $\mu$ m. See also Figure S4.

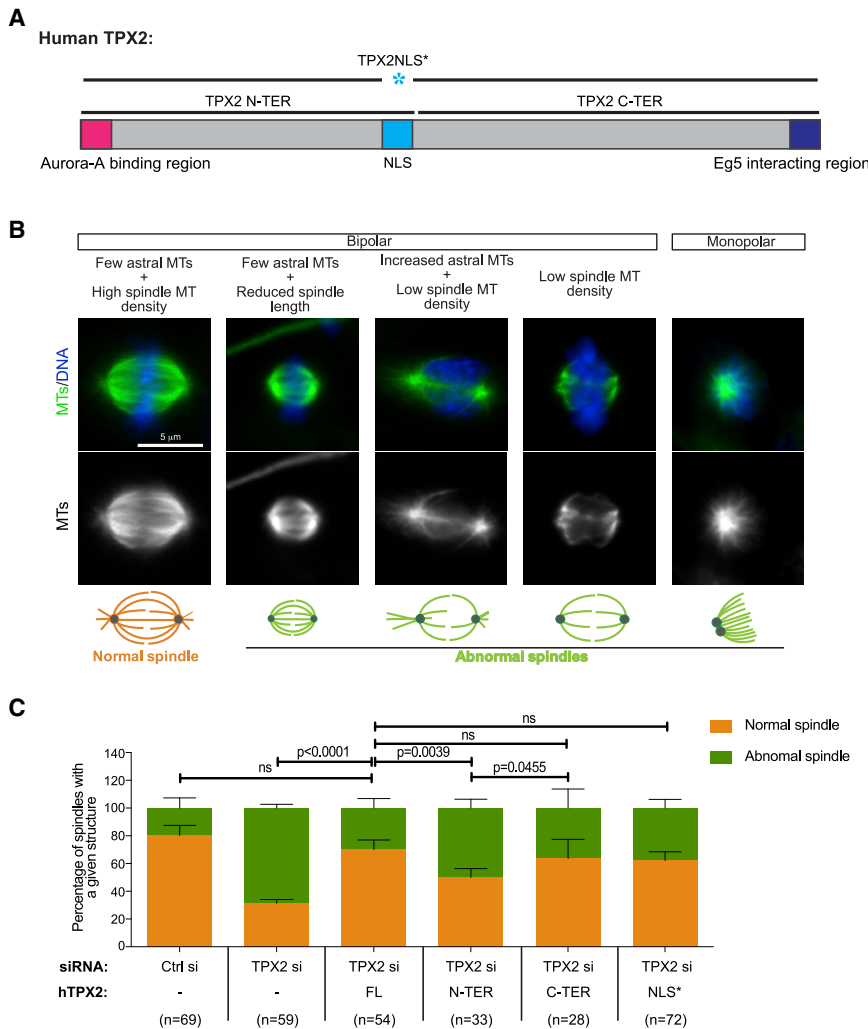


**Figure 5. TPX2 N- and C-Terminal Domains Contribute to Robust Bipolar Spindle Formation**

(A) Schematic representation of human TPX2 protein and its different domains adapted from [42]. (B) Representative images of spindle morphology in E16.5 NSC primary cultures. Monopolar and bipolar spindles with low inner MT density and/or mis-organized MTs were identified as abnormal. (C) Graph bar showing the proportion of E16.5 mitotic NSCs with normal and abnormal spindles after transfection of Ctrl or TPX2 siRNAs with different hTPX2 fragments. The number of NSCs analyzed per condition from 2 replicates is indicated in the graph. Chi-square test was used for statistics. Scale bar, 5  $\mu$ m. See also Figure S5.

the capacity of E13.5 and E16.5 spindles to align and segregate chromosomes upon drug-induced mitotic challenge. First, we challenged mitosis with MPI-0479605, an Mps1 inhibitor, which compromises the spindle assembly checkpoint [45]. We compared the percentage of NSCs in whole-mount cortical explants with misaligned chromosomes at metaphase (Figure 6A) and lagging chromosomes at anaphase (Figure 6B). The frequency of defects was increased after drug incubation in E13.5 NSCs, contrary to E16.5 NSCs (Figures 6C and 6D). E13.5 explants incubated with the DMSO diluent alone, which is a MT stabilizer [46], also displayed high incidence of mitotic errors, as compared to Ctrl (Figures 6C and 6D). We concluded that E13.5 spindles were more prone to mitotic errors upon perturbation of Mps1 activity than E16.5 spindles. As mitotic challenge can impair NSC survival, a phenotype at the origin of microcephaly [14, 16, 20, 47], we compared the levels of apoptosis after Mps1 inhibition at both stages of neurogenesis (Figures 6E and 6F). We confirmed that Mps1 drug-induced mitotic errors resulted in an increase of apoptotic cells at E13.5 as compared to E16.5 (Figures 6E and 6F). Second, we challenged mitosis by impairing the activity of the motor protein CENP-E, which promotes congression and alignment of chromosomes at the metaphase

E13.5 and E16.5 NSCs to mitotic challenge, we partially decreased TPX2 levels in E16.5 brains (Figure 4A) and evaluated the rate of mitotic errors upon Mps1 or CENP-E drug treatments after spindle morphology conversion (24 h post-transfection; Figures 6G, 6H, S6C, and S6D). In agreement with our predictions, the percentage of cells showing mitotic defects in E16.5 brains transfected with TPX2 siRNA was higher than in Ctrl cells (Figures 6G, 6H, S6C, and S6D). Our results show that TPX2 loading status favors accurate cell division upon mitotic challenge.

## DISCUSSION

Our analysis of mitotic spindle architecture in the developing mammalian brain has exposed intrinsic differences in mitotic spindle architecture in NSCs between early and late neurogenic stages. At early stages, the number and length of astral MTs, emanating from the centrosome to contact the cortex, appeared to be greater than at later stages, where astral MTs were more difficult to identify. In contrast, we found that the density of inner spindle MTs, which are responsible for establishing chromosomes interactions, was increased at later neuro-developmental stages in NSCs.

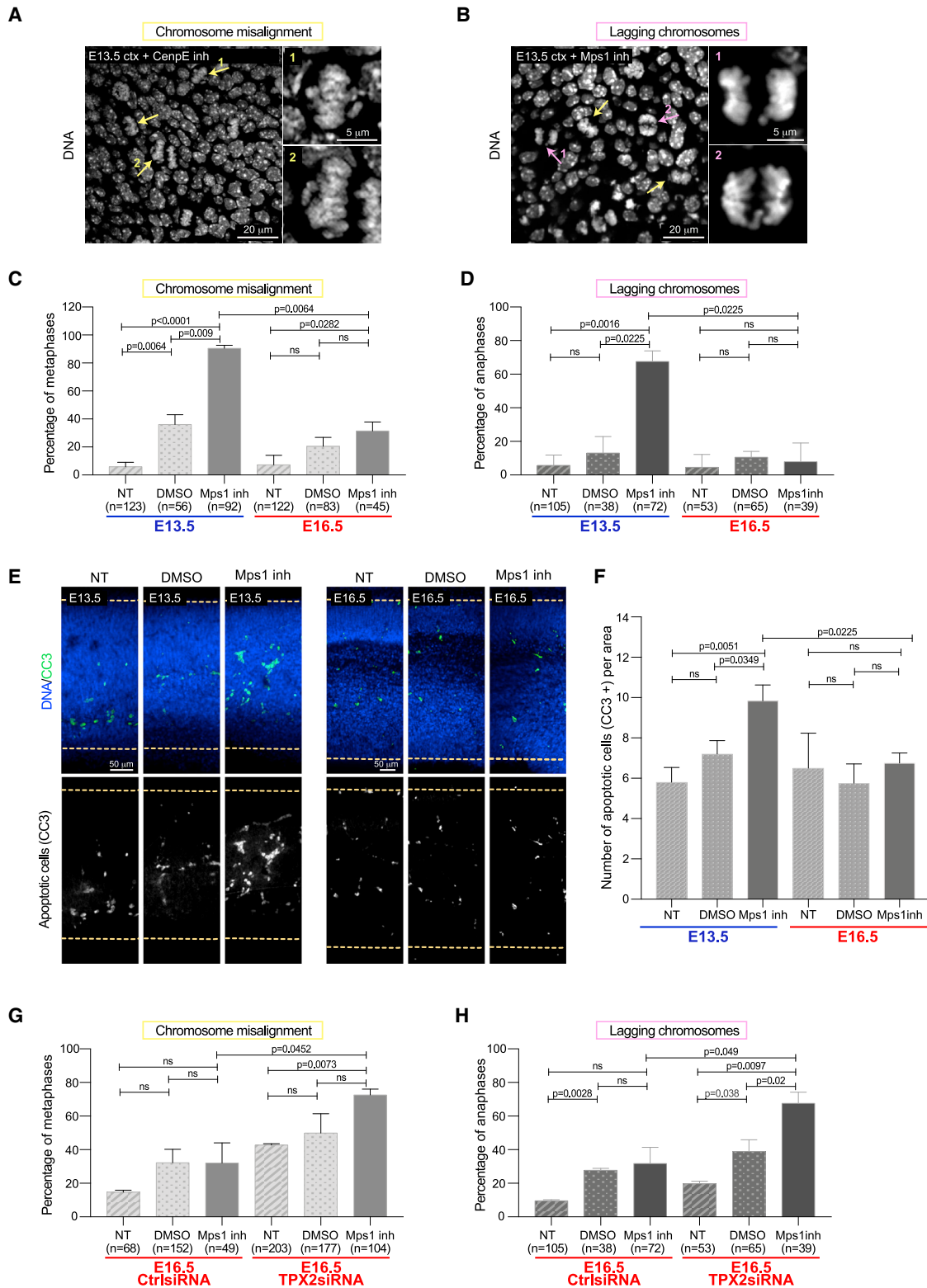


**Figure 6. NSC Spindle Architectures Influence the Rate of Mitotic Errors**

(A and B) Representative confocal images of E13.5 cortical explants after inhibition of CENP-E (A) and Mps1 (B). (Right insets) Higher magnifications of metaphases with misaligned chromosomes (A, yellow arrows) and anaphases with lagging chromosomes (B, purple arrows).

(legend continued on next page)

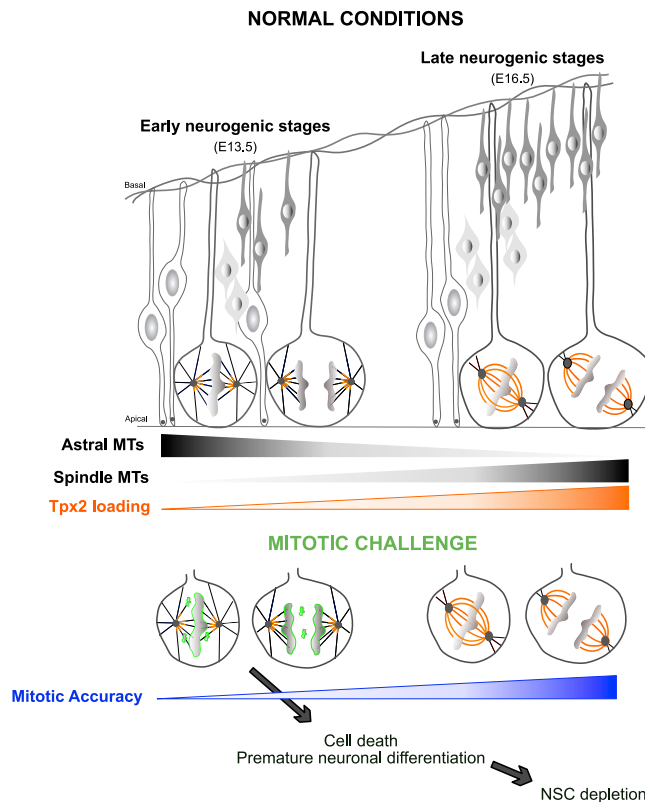


**Figure 7. Variations in NSC Spindle Architectures Influence Susceptibility to Mitotic Errors**

In the mouse neocortex, the mitotic spindle undergoes morphological changes during neurogenesis. Early stages NSC spindles contain many and long astral MTs in comparison to late-stages spindles, and they display reduced MT density in the inner spindle region. These differences in spindle architecture correlate with TPX2 loading status (orange). In unchallenged conditions, E13.5 spindle configuration favors astral MT-cortex interaction to position the spindle during symmetric divisions. Upon mitotic challenge, E13.5 spindle shows higher susceptibility to generate chromosome segregation errors and aneuploid cells. Aneuploid NSCs are eliminated by cell death or premature differentiation, leading to NSC pool depletion.

NSC mitotic spindles are accurately positioned along the apico-basal axis to regulate the axis of division [21]. Our findings and the results described in [23] showing that astral MTs were more abundant at early neurogenesis are justified by their requirement during vertical divisions to expand the population of NSCs and regulate daughter cell positioning. Defects in astral MT nucleation and spindle positioning result in apical NSC loss and lead to brain heterotopia or dysplasia [13, 17, 35, 51–53]. At late neuro-developmental stages, spindles undergo off-vertical divisions and do not anymore require long and robust astral

MT arrays [23], and spindle-size asymmetry might contribute to asymmetric divisions [54].

The spindle is also required to segregate chromosomes correctly in order to prevent the generation of aneuploid cells [55]. We found a higher incidence of chromosome segregation errors when spindle MT density was low. Mitotic errors generate chromosome number imbalance—aneuploidy—associated with limited proliferation capacity [55, 56], premature differentiation [11, 19], and cell death [12, 14–16, 47]. All these conditions contribute to NSC depletion and thus to microcephaly [8–10]. Most likely, the decreased inner MT density typical of early neurogenic stages identified here does not impair mitosis in normal conditions. However, it is possible that, in the presence of hypomorphic microcephaly mutations, error-prone mitosis would be more frequent at early developmental stages (Figure 7). This possibility could be tested by comparing the impact of genetic mutations or Zika virus (ZIKV) infection [57–59] on mitotic fidelity [60, 61] at different neuro-developmental stages. Accordingly, the strongest effect of ZIKV infection was observed at early stages of neurogenesis [62].

We identified TPX2 as one key determinant of spindle morphology. Changes in TPX2 levels are also sufficient to induce variations in spindle architecture and size in *Xenopus* [29]. A slight decrease in TPX2 loading on spindle MTs was sufficient to alter the balance between astral and inner spindle MTs. Our results thus support a model whereby TPX2 loading influences bundling and spatial organization of MTs within NSC spindles (Figure 7). Furthermore, the loading of TPX2 on MTs in interphase NSCs [27] (and this work) appears as a potential regulator of its activity in the subsequent mitosis. Mutations in TPX2 are not found in microcephaly patients. Because TPX2 activity is required in both proliferating and differentiated cells [27, 63, 64], mutations in TPX2 might not be compatible with mammalian development. Accordingly, TPX2-null mutant mice die quite early at around E8 [32].

Our results identify cell-specific spindle morphology tailoring during neuro-development, offering new views on the contribution of spindle assembly to organ homeostasis in health and disease.

## STAR★METHODS

Detailed methods are provided in the online version of this paper and include the following:

- KEY RESOURCES TABLE
- LEAD CONTACT AND MATERIALS AVAILABILITY
- EXPERIMENTAL MODEL AND SUBJECT DETAILS
  - Animals
  - Embryonic mouse neocortical explants

(C and D) Bar graphs showing the proportion of mitotic NSCs with misaligned (C) and lagging (D) chromosomes in E13.5 (blue) and E16.5 (red) cortical explants after treatment (NT, non-treated; DMSO; Mps1 inhibitor [inh]). The number of NSCs analyzed is indicated below. At least 2 brains in 2 independent experiments were analyzed.

(E) Representative images of E13.5 (left panels) and E16.5 (right panels) lateral brain sections after each treatment stained for Cleaved-Caspase 3 (CC3)+ cells. (F) Bar graph showing the proportion of CC3+ cells per area (a.u.). At least 4 sections per brain from 4 brains in 2 replicates were analyzed.

(G and H) Bar graphs showing the percentage of E16.5 NSCs with misaligned (G) and lagging chromosomes (H) after Ctrl or TPX2 siRNAs and the indicated treatments. The number of NSCs analyzed is indicated below. At least 2 brains in 2 replicates were analyzed. For (C), (D), and (F)–(H), error bars represent means  $\pm$  SD and unpaired t tests were used for statistics.

Scale bars, 20  $\mu$ m (A) and 50  $\mu$ m (E). See also Figure S6.

- Human RPE1 cell line culture
- Primary adherent NSC culture and transfection
- **METHOD DETAILS**
  - Cold-based MT depolymerization and repolymerization assays
  - Drug-based assays
  - In utero injection and electroporation procedures
  - Western blot and FACS sorting of NSCs
  - Generation of human TPX2 constructs
  - Generation of antibodies
  - Immunofluorescent staining
- **QUANTIFICATION AND STATISTICAL ANALYSIS**
  - Evaluation of fluorescence intensity index
  - Analysis of spindle architectures
  - Centrosome organization analysis
  - Spindle orientation analysis
  - Quantitative analysis of Western-blots
  - Statistical analysis
- **DATA AND CODE AVAILABILITY**

#### SUPPLEMENTAL INFORMATION

Supplemental Information can be found online at <https://doi.org/10.1016/j.cub.2019.07.061>.

#### ACKNOWLEDGMENTS

We acknowledge the PICT-IBiSA, member of France-Biolmaging (ANR10-INBS-04), and the Nikon Biolmaging Center at I. Curie. We thank C. Janke, F. Francis, A. Dammermann, and D. Cleveland for reagents; C. Lasgi for help with cell sorting; V. Fraiser for microscopy expertise; A. Genovesio for image quantification advice; and SPF facility for animal care. We thank the Basto, Baffet, and Fachinetti labs; A. Bardin; F. Francis; and A. Echard for helpful discussions and or critical reading of the manuscript. We thank PSL and FRM (ECO20170637529) for supporting D.V.-H. INSERM supports V.M. and A.B. The OMX was funded by ERC advanced investigator award EpigenetiX 250367 to E. Heard (I. Curie). This work was supported by CNRS, I. Curie, AICR now WorldWide Cancer (13-0170), ANR (ANR-DIVACEN N°14-CE11), and ERC consolidator ChromoNumber grant 725907 to R.B. The Basto lab is a member of the Labex CelTisPhyBio.

#### AUTHOR CONTRIBUTIONS

D.V.-H., V.M., and R.B. conceived the project, analyzed the data, and wrote the manuscript. D.V.-H. performed most of the experiments. V.M. performed high-resolution microscopy with T.P. and L.L. J.-B.B. and A.B. performed *in utero* injection and electroporation procedures. N.D.S. and C.P. generated tools. R.B. supervised the project.

#### DECLARATION OF INTERESTS

The authors declare no competing interests.

Received: October 19, 2018

Revised: May 31, 2019

Accepted: July 19, 2019

Published: September 5, 2019

#### REFERENCES

1. Wadsworth, P., Lee, W.L., Murata, T., and Baskin, T.I. (2011). Variations on theme: spindle assembly in diverse cells. *Protoplasma* 248, 439–446.
2. Helmke, K.J., Heald, R., and Wilbur, J.D. (2013). Interplay between spindle architecture and function. *Int. Rev. Cell Mol. Biol.* 306, 83–125.
3. Crowder, M.E., Strzelecka, M., Wilbur, J.D., Good, M.C., von Dassow, G., and Heald, R. (2015). A comparative analysis of spindle morphometrics across metazoans. *Curr. Biol.* 25, 1542–1550.
4. Farhadifar, R., Baer, C.F., Valfort, A.C., Andersen, E.C., Müller-Reichert, T., Delattre, M., and Needleman, D.J. (2015). Scaling, selection, and evolutionary dynamics of the mitotic spindle. *Curr. Biol.* 25, 732–740.
5. Götz, M., and Huttner, W.B. (2005). The cell biology of neurogenesis. *Nat. Rev. Mol. Cell Biol.* 6, 777–788.
6. Fernández, V., Llinares-Benadero, C., and Borrell, V. (2016). Cerebral cortex expansion and folding: what have we learned? *EMBO J.* 35, 1021–1044.
7. Jayaraman, D., Bae, B.I., and Walsh, C.A. (2018). The genetics of primary microcephaly. *Annu. Rev. Genomics Hum. Genet.* 19, 177–200.
8. Nano, M., and Basto, R. (2017). Consequences of centrosome dysfunction during brain development. *Adv. Exp. Med. Biol.* 1002, 19–45.
9. Thornton, G.K., and Woods, C.G. (2009). Primary microcephaly: do all roads lead to Rome? *Trends Genet.* 25, 501–510.
10. Woods, C.G., and Basto, R. (2014). Microcephaly. *Curr. Biol.* 24, R1109–R1111.
11. Gogondeau, D., Siudeja, K., Gambarotto, D., Pennetier, C., Bardin, A.J., and Basto, R. (2015). Aneuploidy causes premature differentiation of neural and intestinal stem cells. *Nat. Commun.* 6, 8894.
12. Rujano, M.A., Sanchez-Pulido, L., Pennetier, C., le Dez, G., and Basto, R. (2013). The microcephaly protein Asp regulates neuroepithelium morphogenesis by controlling the spatial distribution of myosin II. *Nat. Cell Biol.* 15, 1294–1306.
13. Insolera, R., Bazzi, H., Shao, W., Anderson, K.V., and Shi, S.H. (2014). Cortical neurogenesis in the absence of centrioles. *Nat. Neurosci.* 17, 1528–1535.
14. Lizaraga, S.B., Margossian, S.P., Harris, M.H., Campagna, D.R., Han, A.P., Blevins, S., Mudbhary, R., Barker, J.E., Walsh, C.A., and Fleming, M.D. (2010). Cdk5rap2 regulates centrosome function and chromosome segregation in neuronal progenitors. *Development* 137, 1907–1917.
15. Marjanović, M., Sánchez-Huertas, C., Terré, B., Gómez, R., Scheel, J.F., Pacheco, S., Knobel, P.A., Martínez-Marchal, A., Aivio, S., Palenzuela, L., et al. (2015). CEP63 deficiency promotes p53-dependent microcephaly and reveals a role for the centrosome in meiotic recombination. *Nat. Commun.* 6, 7676.
16. Marthiens, V., Rujano, M.A., Pennetier, C., Tessier, S., Paul-Gilloteaux, P., and Basto, R. (2013). Centrosome amplification causes microcephaly. *Nat. Cell Biol.* 15, 731–740.
17. Johnson, M.B., Sun, X., Kodani, A., Borges-Monroy, R., Girsakis, K.M., Ryu, S.C., Wang, P.P., Patel, K., Gonzalez, D.M., Woo, Y.M., et al. (2018). Aspm knockout ferret reveals an evolutionary mechanism governing cerebral cortical size. *Nature* 556, 370–375.
18. Bazzi, H., and Anderson, K.V. (2014). Acentriolar mitosis activates a p53-dependent apoptosis pathway in the mouse embryo. *Proc. Natl. Acad. Sci. USA* 111, E1491–E1500.
19. Buchman, J.J., Tseng, H.C., Zhou, Y., Frank, C.L., Xie, Z., and Tsai, L.H. (2010). Cdk5rap2 interacts with pericentrin to maintain the neural progenitor pool in the developing neocortex. *Neuron* 66, 386–402.
20. Pilaz, L.J., McMahon, J.J., Miller, E.E., Lennox, A.L., Suzuki, A., Salmon, E., and Silver, D.L. (2016). Prolonged mitosis of neural progenitors alters cell fate in the developing brain. *Neuron* 89, 83–99.
21. Taverna, E., Götz, M., and Huttner, W.B. (2014). The cell biology of neurogenesis: toward an understanding of the development and evolution of the neocortex. *Annu. Rev. Cell Dev. Biol.* 30, 465–502.
22. di Pietro, F., Echard, A., and Morin, X. (2016). Regulation of mitotic spindle orientation: an integrated view. *EMBO Rep.* 17, 1106–1130.

23. Mora-Bermúdez, F., Matsuzaki, F., and Huttner, W.B. (2014). Specific polar subpopulations of astral microtubules control spindle orientation and symmetric neural stem cell division. *eLife* 3, e02875.
24. Rujano, M.A., Basto, R., and Marthiens, V. (2015). New insights into centrosome imaging in *Drosophila* and mouse neuroepithelial tissues. In *Methods in Cell Biology*, Chapter 12, *Volume 129*, R. Basto, and K. Oegema, eds. (Academic Press), pp. 211–227.
25. Janke, C. (2014). The tubulin code: molecular components, readout mechanisms, and functions. *J. Cell Biol.* 206, 461–472.
26. Gruss, O.J., Wittmann, M., Yokoyama, H., Pepperkok, R., Kufer, T., Silljé, H., Karsenti, E., Mattaj, I.W., and Vernos, I. (2002). Chromosome-induced microtubule assembly mediated by TPX2 is required for spindle formation in HeLa cells. *Nat. Cell Biol.* 4, 871–879.
27. Kosodo, Y., Suetsugu, T., Suda, M., Mimori-Kiyosue, Y., Toida, K., Baba, S.A., Kimura, A., and Matsuzaki, F. (2011). Regulation of interkinetic nuclear migration by cell cycle-coupled active and passive mechanisms in the developing brain. *EMBO J.* 30, 1690–1704.
28. Schatz, C.A., Santarella, R., Hoenger, A., Karsenti, E., Mattaj, I.W., Gruss, O.J., and Carazo-Salas, R.E. (2003). Importin alpha-regulated nucleation of microtubules by TPX2. *EMBO J.* 22, 2060–2070.
29. Helmke, K.J., and Heald, R. (2014). TPX2 levels modulate meiotic spindle size and architecture in *Xenopus* egg extracts. *J. Cell Biol.* 206, 385–393.
30. Ma, N., Titus, J., Gable, A., Ross, J.L., and Wadsworth, P. (2011). TPX2 regulates the localization and activity of Eg5 in the mammalian mitotic spindle. *J. Cell Biol.* 195, 87–98.
31. Maliga, Z., Kapoor, T.M., and Mitchison, T.J. (2002). Evidence that monastrol is an allosteric inhibitor of the mitotic kinesin Eg5. *Chem. Biol.* 9, 989–996.
32. Aguirre-Portolés, C., Bird, A.W., Hyman, A., Cañamero, M., Pérez de Castro, I., and Malumbres, M. (2012). Tpx2 controls spindle integrity, genome stability, and tumor development. *Cancer Res.* 72, 1518–1528.
33. Bird, A.W., and Hyman, A.A. (2008). Building a spindle of the correct length in human cells requires the interaction between TPX2 and Aurora A. *J. Cell Biol.* 182, 289–300.
34. Reiner, O., Gorelik, A., and Greenman, R. (2012). Use of RNA interference by in utero electroporation to study cortical development: the example of the doublecortin superfamily. *Genes (Basel)* 3, 759–778.
35. Postiglione, M.P., Jüschke, C., Xie, Y., Haas, G.A., Charalambous, C., and Knoblich, J.A. (2011). Mouse inscuteable induces apical-basal spindle orientation to facilitate intermediate progenitor generation in the developing neocortex. *Neuron* 72, 269–284.
36. Sun, T., Wang, X.-J., Xie, S.-S., Zhang, D.-L., Wang, X.-P., Li, B.-Q., Ma, W., and Xin, H. (2011). A comparison of proliferative capacity and passing potential between neural stem and progenitor cells in adherent and neurosphere cultures. *Int. J. Dev. Neurosci.* 29, 723–731.
37. Alfaro-Aco, R., Thawani, A., and Petry, S. (2017). Structural analysis of the role of TPX2 in branching microtubule nucleation. *J. Cell Biol.* 216, 983–997.
38. Brunet, S., Sardon, T., Zimmerman, T., Wittmann, T., Pepperkok, R., Karsenti, E., and Vernos, I. (2004). Characterization of the TPX2 domains involved in microtubule nucleation and spindle assembly in *Xenopus* egg extracts. *Mol. Cell Biol.* 24, 5318–5328.
39. Bayliss, R., Sardon, T., Vernos, I., and Conti, E. (2003). Structural basis of Aurora-A activation by TPX2 at the mitotic spindle. *Mol. Cell* 12, 851–862.
40. Eckerdt, F., Eysers, P.A., Lewellyn, A.L., Prigent, C., and Maller, J.L. (2008). Spindle pole regulation by a discrete Eg5-interacting domain in TPX2. *Curr. Biol.* 18, 519–525.
41. Gruss, O.J., Carazo-Salas, R.E., Schatz, C.A., Guarguagliini, G., Kast, J., Wilm, M., Le Bot, N., Vernos, I., Karsenti, E., and Mattaj, I.W. (2001). Ran induces spindle assembly by reversing the inhibitory effect of importin alpha on TPX2 activity. *Cell* 104, 83–93.
42. Zhang, R., Roostalu, J., Surrey, T., and Nogales, E. (2017). Structural insight into TPX2-stimulated microtubule assembly. *eLife* 6, e30959.
43. Wittmann, T., Wilm, M., Karsenti, E., and Vernos, I. (2000). TPX2, a novel *xenopus* MAP involved in spindle pole organization. *J. Cell Biol.* 149, 1405–1418.
44. Roostalu, J., Cade, N.I., and Surrey, T. (2015). Complementary activities of TPX2 and chTOG constitute an efficient importin-regulated microtubule nucleation module. *Nat. Cell Biol.* 17, 1422–1434.
45. Tardif, K.D., Rogers, A., Cassiano, J., Roth, B.L., Cimbara, D.M., McKinnon, R., Peterson, A., Douce, T.B., Robinson, R., Dorweiler, I., et al. (2011). Characterization of the cellular and antitumor effects of MPI-0479605, a small-molecule inhibitor of the mitotic kinase Mps1. *Mol. Cancer Ther.* 10, 2267–2275.
46. Algaier, J., and Himes, R.H. (1988). The effects of dimethyl sulfoxide on the kinetics of tubulin assembly. *Biochim. Biophys. Acta* 954, 235–243.
47. McIntyre, R.E., Lakshminarasimhan Chavali, P., Ismail, O., Carragher, D.M., Sanchez-Andrade, G., Forment, J.V., Fu, B., Del Castillo Velasco-Herrera, M., Edwards, A., van der Weyden, L., et al.; Sanger Mouse Genetics Project (2012). Disruption of mouse Cenpj, a regulator of centriole biogenesis, phenocopies Seckel syndrome. *PLoS Genet.* 8, e1003022.
48. Gudimchuk, N., Vitre, B., Kim, Y., Kiyatkin, A., Cleveland, D.W., Ataullakhanov, F.I., and Grishchuk, E.L. (2013). Kinetochore kinesin CENP-E is a processive bi-directional tracker of dynamic microtubule tips. *Nat. Cell Biol.* 15, 1079–1088.
49. Mirzaa, G.M., Vitre, B., Carpenter, G., Abramowicz, I., Gleeson, J.G., Paciorkowski, A.R., Cleveland, D.W., Dobyns, W.B., and O'Driscoll, M. (2014). Mutations in CENPE define a novel kinetochore-centromeric mechanism for microcephalic primordial dwarfism. *Hum. Genet.* 133, 1023–1039.
50. Bennett, A., Bechi, B., Tighe, A., Thompson, S., Procter, D.J., and Taylor, S.S. (2015). Cenp-E inhibitor GSK923295: novel synthetic route and use as a tool to generate aneuploidy. *Oncotarget* 6, 20921–20932.
51. Fish, J.L., Kosodo, Y., Enard, W., Pääbo, S., and Huttner, W.B. (2006). Aspm specifically maintains symmetric proliferative divisions of neuroepithelial cells. *Proc. Natl. Acad. Sci. USA* 103, 10438–10443.
52. Konno, D., Shioi, G., Shitamukai, A., Mori, A., Kiyonari, H., Miyata, T., and Matsuzaki, F. (2008). Neuroepithelial progenitors undergo LGN-dependent planar divisions to maintain self-renewability during mammalian neurogenesis. *Nat. Cell Biol.* 10, 93–101.
53. Yingling, J., Youn, Y.H., Darling, D., Toyo-Oka, K., Pramparo, T., Hirotsune, S., and Wynshaw-Boris, A. (2008). Neuroepithelial stem cell proliferation requires LIS1 for precise spindle orientation and symmetric division. *Cell* 132, 474–486.
54. Delaunay, D., Cortay, V., Patti, D., Knoblauch, K., and Dehay, C. (2014). Mitotic spindle asymmetry: a Wnt/PCP-regulated mechanism generating asymmetrical division in cortical precursors. *Cell Rep.* 6, 400–414.
55. Santaguida, S., and Amon, A. (2015). Short- and long-term effects of chromosome mis-segregation and aneuploidy. *Nat. Rev. Mol. Cell Biol.* 16, 473–485.
56. Santaguida, S., Richardson, A., Iyer, D.R., M'Saad, O., Zasadil, L., Knouse, K.A., Wong, Y.L., Rhind, N., Desai, A., and Amon, A. (2017). Chromosome mis-segregation generates cell-cycle-arrested cells with complex karyotypes that are eliminated by the immune system. *Dev. Cell* 41, 638–651.e5.
57. Cauchemez, S., Besnard, M., Bompard, P., Dub, T., Guillemette-Artur, P., Eyrolle-Guignot, D., Salje, H., Van Kerkhove, M.D., Abadie, V., Garel, C., et al. (2016). Association between Zika virus and microcephaly in French Polynesia, 2013–15: a retrospective study. *Lancet* 387, 2125–2132.
58. Cugola, F.R., Fernandes, I.R., Russo, F.B., Freitas, B.C., Dias, J.L., Guimaraes, K.P., Benazzato, C., Almeida, N., Pignatari, G.C., Romero, S., et al. (2016). The Brazilian Zika virus strain causes birth defects in experimental models. *Nature* 534, 267–271.
59. Dang, J., Tiwari, S.K., Lichinchi, G., Qin, Y., Patil, V.S., Eroshkin, A.M., and Rana, T.M. (2016). Zika virus depletes neural progenitors in human

- cerebral organoids through activation of the innate immune receptor TLR3. *Cell Stem Cell* *19*, 258–265.
60. Souza, B.S., Sampaio, G.L., Pereira, C.S., Campos, G.S., Sardi, S.I., Freitas, L.A., Figueira, C.P., Paredes, B.D., Nonaka, C.K., Azevedo, C.M., et al. (2016). Zika virus infection induces mitosis abnormalities and apoptotic cell death of human neural progenitor cells. *Sci. Rep.* *6*, 39775.
  61. Wolf, B., Diop, F., Ferraris, P., Wichit, S., Busso, C., Missé, D., and Gönczy, P. (2017). Zika virus causes supernumerary foci with centriolar proteins and impaired spindle positioning. *Open Biol.* *7*, 160231.
  62. Qian, X., Nguyen, H.N., Song, M.M., Hadiono, C., Ogden, S.C., Hammack, C., Yao, B., Hamersky, G.R., Jacob, F., Zhong, C., et al. (2016). Brain-region-specific organoids using mini-bioreactors for modeling ZIKV exposure. *Cell* *165*, 1238–1254.
  63. Wadsworth, P. (2015). Tpx2. *Curr. Biol.* *25*, R1156–R1158.
  64. Chen, W.S., Chen, Y.J., Huang, Y.A., Hsieh, B.Y., Chiu, H.C., Kao, P.Y., Chao, C.Y., and Hwang, E. (2017). Ran-dependent TPX2 activation promotes centrosomal microtubule nucleation in neurons. *Sci. Rep.* *7*, 42297.
  65. Brown, K.D., Wood, K.W., and Cleveland, D.W. (1996). The kinesin-like protein CENP-E is kinetochore-associated throughout poleward chromosome segregation during anaphase-A. *J. Cell Sci.* *109*, 961–969.
  66. Kielar, M., Tuy, F.P., Bizzotto, S., Lebrand, C., de Juan Romero, C., Poirier, K., Oegema, R., Mancini, G.M., Bahi-Buisson, N., Olasso, R., et al. (2014). Mutations in Eml1 lead to ectopic progenitors and neuronal heterotopia in mouse and human. *Nat. Neurosci.* *17*, 923–933.
  67. Gustafsson, M.G., Shao, L., Carlton, P.M., Wang, C.J., Golubovskaya, I.N., Cande, W.Z., Agard, D.A., and Sedat, J.W. (2008). Three-dimensional resolution doubling in wide-field fluorescence microscopy by structured illumination. *Biophys. J.* *94*, 4957–4970.
  68. Baffet, A.D., Carabalona, A., Dantas, T.J., Doobin, D.D., Hu, D.J., and Vallee, R.B. (2016). Cellular and subcellular imaging of motor protein-based behavior in embryonic rat brain. *Methods Cell Biol.* *131*, 349–363.
  69. Sonnen, K.F., Schermelleh, L., Leonhardt, H., and Nigg, E.A. (2012). 3D-structured illumination microscopy provides novel insight into architecture of human centrosomes. *Biol. Open* *1*, 965–976.
  70. Haydar, T.F., Ang, E., Jr., and Rakic, P. (2003). Mitotic spindle rotation and mode of cell division in the developing telencephalon. *Proc. Natl. Acad. Sci. USA* *100*, 2890–2895.

## STAR★METHODS

### KEY RESOURCES TABLE

REAGENT or RESOURCE	SOURCE	IDENTIFIER
<b>Antibodies</b>		
Mouse Acetylated-tubulin	Sigma	Cat#T7451; RRID: AB_609894
Rabbit Afadin antibody	Abcam	Cat#ab11337; RRID: AB_297943
Mouse alpha-tubulin antibody, clone DM1a	Sigma	Cat#T6199; RRID: AB_477583
Mouse beta-tubulin isotype III	Sigma	Cat#T8660; RRID: AB_477590
Rabbit Cleaved caspase-3 (CC3)	Cell Signaling	Cat#9661; RRID: AB_2341188
Rabbit Cdk5rap2	Bethyl Laboratories	Cat#IHC-00063; RRID: AB_2076863
Rabbit CENP-E	Laboratory of D. W. Cleveland (LICR, La Jolla, USA); [65]	N/A
Rabbit Centrin-3	This paper	N/A
Human Centromere	Antibodies	Cat#15-235-0001; RRID: AB_2797146
Rabbit Cep135	This paper	N/A
Rabbit Cep192	This paper	N/A
Rabbit Detyrosinated tubulin	Merck	Cat#AB3201; RRID: AB_303601
Rabbit Eg5	Novus Biologicals	NB500-181; RRID: AB_10002881
Chicken GFP	Abcam	ab13970; RRID: AB_300798
Mouse gamma-tubulin (clone GTU88)	Sigma	T5326; RRID: AB_532292
Rabbit HSET	This paper	N/A
Mouse Nestin antibody	BD Bioscience	556309; RRID: AB_396354
Rabbit NeuN	Abcam	ab177487; RRID: AB_2532109
Rabbit NuMA	Novus Biologicals	NB500-174; RRID: AB_10002562
Rabbit Pax6	Millipore	AB2237; RRID: AB_2270373
Rabbit Pericentrin	Abcam	ab4448; RRID: AB_304461
Rabbit RCC1	Proteintech	22142-1-AP; RRID: AB_11183045
Goat Sox2	R and D Systems	AF2018; RRID: AB_355110
Rabbit TPX2 antibody	Abnova	Cat#PAB11993; RRID: AB_1716384
Rat Tyrosinated tubulin	Laboratory of C.Janke, Curie Institute, Paris, France	N/A
Peroxidase AffiniPure Goat Anti-Mouse IgG (H+L)	Jackson ImmunoResearch	115-035-003; RRID: AB_10015289
Goat anti-Rabbit IgG (H+L) Cross-Adsorbed Secondary Antibody, HRP	Molecular Probes	G21234; RRID: AB_2536530
Goat anti-mouse IgG (H+L) Highly Cross-Adsorbed Secondary Antibody, Alexa Fluor 488-conjugated	Molecular Probes	Cat#A-11029; RRID: AB_138404
Goat anti-mouse IgG (H+L) Highly Cross-Adsorbed Secondary Antibody, Alexa Fluor 546-conjugated	Molecular Probes	Cat#A-11030; RRID: AB_144695
Goat anti-mouse IgG (H+L) Highly Cross-Adsorbed Secondary Antibody, Alexa Fluor 647-conjugated	Molecular Probes	Cat#A-21236; RRID: AB_141725
Goat anti-rabbit IgG (H+L) Highly Cross-Adsorbed Secondary Antibody, Alexa Fluor 488-conjugated	Molecular Probes	Cat#A-11034; RRID: AB_2576217
Goat anti-rabbit IgG (H+L) Highly Cross-Adsorbed Secondary Antibody, Alexa Fluor 546-conjugated	Molecular Probes	Cat#A-11035; RRID: AB_143051
Goat anti-rabbit IgG (H+L) Highly Cross-Adsorbed Secondary Antibody, Alexa Fluor 647-conjugated	Molecular Probes	Cat#A-21245; RRID: AB_141775
Donkey anti-rabbit IgG (H+L) Highly Cross-Adsorbed Secondary Antibody, Alexa Fluor 568-conjugated	Molecular Probes	Cat#A-10042; RRID: AB_2534017

(Continued on next page)

**Continued**

REAGENT or RESOURCE	SOURCE	IDENTIFIER
Goat anti-chicken IgY (H+L) Highly Cross-Adsorbed Secondary Antibody, Alexa Fluor 488-conjugated	Molecular Probes	Cat#A-11039; RRID: AB_142924
Goat anti-rat IgG (H+L) Cross-Adsorbed Secondary Antibody, Alexa Fluor 488-conjugated	Molecular Probes	Cat#A-A11006; RRID: AB_141373
Donkey anti-goat IgG (H+L) Secondary Antibody, Alexa Fluor 647-conjugated	Molecular Probes	Cat#A-21447; RRID: AB_141844
Goat anti-human IgG (H+L) Secondary Antibody, Alexa Fluor 647-conjugated	Molecular Probes	Cat#A-A21445; RRID: AB_141843
4',6-diamidino-2-phenylindole (DAPI)	Molecular Probes	Cat#D1306; RRID: AB_2629482
<b>Bacterial and Virus Strains</b>		
Competent <i>E.Coli</i> bacteria, strain DH5a	ThermoFisher Scientific	Cat#18258012
Competent <i>E.Coli</i> bacteria, strain C41	ThermoFisher Scientific	N/A
<b>Biological Samples</b>		
Embryonic mouse cortical explants	This paper	N/A
Primary cultures of embryonic NSCs	This paper	N/A
<b>Chemicals, Peptides, and Recombinant Proteins</b>		
Forene (isoflurane)	abbvie	Cat#B506
Fibroblast growth factor-Basic human (bFGF)	Sigma	Cat#F0291
Epidermal growth factor-human (hEGF)	Sigma	Cat#E9644
Poly-D-Lysine Hydrobromide, 70000-150000 MW	Sigma	Cat#P6407
Fibronectin	Sigma	Cat#F1141
Accutase	Sigma	Cat#A6964
Monastrol (inhibitor of Eg5 motor protein)	Selleckchem	Cat#S8439
GSK923295 (inhibitor of Cenp-E motor protein)	Selleckchem	Cat#S7090
MPI-0479605 (inhibitor of Mps1)	Selleckchem	Cat#S7488
Dimethyl Sulfoxide Anhydrous (DMSO)	Sigma	Cat#276855
FastGreen	Sigma	Cat#68724
<b>Critical Commercial Assays</b>		
Phusion high-fidelity PCR kit	New England Biolabs	Cat#E0553S
QIAquick PCR Purification Kit	ThermoFisher Scientific	Cat#28104
DNA Ligation Kit	Takara	Cat#6023
Q5 Site-Directed Mutagenesis Kit	New England Biolabs	Cat#E0554S
Endofree Plasmid Maxi Kit	QIAGEN	Cat#12362
Mouse NSC nucleofactor kit	Lonza	Cat#VPG-1004
Gateway cloning system	ThermoFisher Scientific	Cat#12535-019
Amylose resin	New England Biolabs	Cat#E8021L
Affigel 10 columns	BioRad	Cat#153-6052
Affigel 15 columns	BioRad	Cat#153-6046
PlasmoTest-Mycoplasma Detection Kit	InvivoGen	Cat#rep-pt1
Powerplex16 HS kit	Promega	Cat#DC2101
<b>Deposited Data</b>		
<i>Mus musculus</i> Centrin3, mRNA,	NCBI	<a href="https://www.ncbi.nlm.nih.gov/nuccore/NM_007684.3">https://www.ncbi.nlm.nih.gov/nuccore/NM_007684.3</a>
<i>Mus musculus</i> centrosomal protein 135 (Cep135), mRNA	NCBI	<a href="https://www.ncbi.nlm.nih.gov/nuccore/NM_199032.3">https://www.ncbi.nlm.nih.gov/nuccore/NM_199032.3</a>
<i>Mus musculus</i> kinesin family member C1 (Kifc1), mRNA	NCBI	<a href="https://www.ncbi.nlm.nih.gov/nuccore/NM_001195298.1">https://www.ncbi.nlm.nih.gov/nuccore/NM_001195298.1</a>
Homo sapiens TPX2, microtubule nucleation factor (TPX2), mRNA	NCBI	<a href="https://www.ncbi.nlm.nih.gov/nuccore/NM_012112.4">https://www.ncbi.nlm.nih.gov/nuccore/NM_012112.4</a>

(Continued on next page)

**Continued**

REAGENT or RESOURCE	SOURCE	IDENTIFIER
Experimental Models: Cell Lines		
hTERT RPE-1 cells	ATCC	CRL-4000; RRID: CVCL_4388
Experimental Models: Organisms/Strains		
Pregnant females C57Bl6/N between E10.5 and E18.5 days of gestation	Charles River (France)	N/A
Male and female embryos between E10.5 and E18.5 days of gestation	Charles River (France)	N/A
Oligonucleotides		
ON-TARGET plus Mouse Tpx2 (72119) siRNA - SMART POOL	Dharmacon	Cat#L-055634-01-0005
ON-TARGET plus Non-targeting Pool siRNA	Dharmacon	Cat#D-001810-10-05
Primer: hTPX2FL forward, 5'-CGCGAAGCTTCAA TGTCACAAGTTAAAAGC-3'	This paper	N/A
Primer: hTPX2FL reverse, 5'-CGCGGGTACCTTA GCAGTGGAATCGAGTGG-3'	This paper	N/A
hTPX2CT forward, 5'-CGCGAAGCTTCAGTACTG CAAACCAACAC-3'	This paper	N/A
hTPX2NT forward, 5'-CGCGCTCGAGCAATGTCA CAAGTTAAAAGC-3'	This paper	N/A
hTPX2NT reverse, 5'-CGCGGGTACCTTAAGGAG TCTGTGGGTCTC-3'	This paper	N/A
hTPX2NLS* forward, 5'-CTTGCACAGCAAGTTG AAGACTTCCATGCAGCAACCCCTAACAGATATC ATTTGAGGAGCAAG-3'	This paper	N/A
hTPX2NLS* reverse, 5'-CTTGCACAGCAAGTTGA AGACTTCCATGCAGCAACCCCTAACAGATATCA TTTGAGGAGCAAG-3'	This paper	N/A
mCentrin3/aa:1-168 forward, 5'-GGGGACAAGT TTGTACAAAAAGCAGGCTTCATGAGTTTAGC TCTGAGAGGTGAG-3'	This paper	N/A
mCentrin3/aa:1-168 reverse, 5'-GGGACCACTT TGTACAAGAAAGCTGGGTCTTATATGTCACCA GTCATAATAGC-3'	This paper	N/A
mCep135/aa:936-1141 forward, 5'-GGGGACAAG TTTGTACAAAAAGCAGGCTTCAATGCACATCA CGCATACGAGTCT-3'	This paper	N/A
mCep135/aa:936-1141 reverse, 5'-GGGGACC ACTTTGTACAAGAAAGCTGGGTCTTATGCATT TATATGATCAGGAGT-3'	This paper	N/A
hCep192/aa:1-210 forward, 5'-GGGACAAGTTT GTACAAAAAGCAATGGAAGATTTTCGAGGTAT AGCA-3'	This paper	N/A
hCep192/aa:1-210 reverse, 5'-GGGACCACAT TTGTACAAGAAAGCTGGGTCTCAATCTTCCA AGCTTGTCGGTAAGAT-3'	This paper	N/A
mHSET/aa:1-227 forward, 5'-GGGGACAAGTTT GTACAAAAAGCAGGTTTCATGGACGTGCAGG CGCAGAGGCCA-3'	This paper	N/A
mHSET/aa:1-227 reverse, 5'-GGGGACCACTT TGTACAAGAAAGCTGGGTCTTAAAGCAGCCTT TCCCTGGTACCCAG -3'	This paper	N/A

(Continued on next page)

**Continued**

REAGENT or RESOURCE	SOURCE	IDENTIFIER
<b>Recombinant DNA</b>		
pBLBP-EGFP plasmid	Laboratory of F.Francis (IFM, Paris, France); [66]	N/A
pEGFP-C1 plasmid	Clontech	<a href="https://www.addgene.org/vector-database/2487">https://www.addgene.org/vector-database/2487</a>
TPX2 (NM_012112) Human untagged clone	Origene	Cat#SC115515
<i>Mus musculus</i> Centrin3; IMAGE clone ID: 30019209	Thermo Fisher Scientific Biosciences	Cat#MMM1013-202805556
<i>Mus musculus</i> Cep135; IMAGE clone ID: 6852711	Thermo Fisher Scientific Biosciences	Cat#MMM1013-202859840
hCep192 containing plasmid	Laboratory of A.Dammermann (MPL, Vienna, Austria)	N/A
<i>Mus musculus</i> Kifc1/HSET; IMAGE clone ID: 30841951	Thermo Fisher Scientific Biosciences	Cat#MMM1013-202780075
<b>Software and Algorithms</b>		
Fiji software for image analysis	Open source image processing software	<a href="http://imagej.net/Contributors">http://imagej.net/Contributors</a> ; RRID: SCR_002285
NIS Elements viewer software v4.3.02	Nikon; [67]	N/A
Prism software for graphs and statistical analysis, version 7	GraphPad Software	N/A
Affinity Designer	Affinity	<a href="https://affinity.serif.com/en-us/designer/">https://affinity.serif.com/en-us/designer/</a> RRID: SCR_016952
Affinity Photo	Affinity	<a href="https://affinity.serif.com/en-us/photo/">https://affinity.serif.com/en-us/photo/</a> RRID: SCR_016951
<b>Other</b>		
DMEM/HamF12 powder	GIBCO	Cat#42400-028
DMEM/F12	GIBCO	Cat#11320-033
Sodium bicarbonate	Sigma	Cat#S5761
Glucose	Sigma	Cat#G6152
B27 supplement w/o vitamin A	ThermoFisher Scientific	Cat#12587-010
N2 supplement	GIBCO	Cat#17502-048
Fetal Bovine Serum (FBS)	GIBCO	Cat#1027016
Horse Serum (HS)	GIBCO	Cat#16050122
Penicillin/streptomycin	GIBCO	Cat#15140-122
Amphotericin B (fungizone)	Sigma	Cat#A2942
10S Voltalef oil	VWR BDH Prolabo	Cat#9002-83-9

**LEAD CONTACT AND MATERIALS AVAILABILITY**

Further information and requests for resources and reagents should be directed to and will be fulfilled by the Lead contact Renata Basto ([renata.basto@curie.fr](mailto:renata.basto@curie.fr)).

There are no restrictions to the availability of reagents generated in this study.

**EXPERIMENTAL MODEL AND SUBJECT DETAILS**

**Animals**

For animal care, we followed the European and French National Regulation for the Protection of Vertebrate Animals used for Experimental and other Scientific Purposes (Directive 2010/63; French Decree 2013-118). The project was authorized and benefited from guidance of the Animal Welfare Body, Research Centre, Curie Institute. All mice were kept at the Curie I. Specific Pathogen Free (SPF) animal facility for breeding. C57Bl6/N pregnant females were purchased from Charles River Laboratories (France).

For all pregnant females, the day of mating was referred to 0.5 day of gestation (E0.5). Pregnant females from embryonic day 10.5 (E10.5) to embryonic day 18.5 (E18.5) were used. They were anaesthetized by inhalation of isoflurane (Forene, Abbvie, B506) before being sacrificed by cervical dislocation. Embryos were collected after caesarean section. Embryos from both sexes were indistinctly used in all the experimental procedures.

### Embryonic mouse neocortical explants

Dorsal telencephalons (referred after as cerebral cortices or cortical explants) of wild-type C57Bl6/N embryos were dissected at different stages of neurogenesis (from E10.5 to E18.5). Preparations of mouse embryonic brain tissues for *en face view* analysis are described in details in [24]. To prevent microtubule (MT) depolymerization, cerebral cortices were dissected at room temperature (RT) in 37°C pre-warmed DMEM/HamF12 medium (GIBCO, 42400-028), supplemented with glucose (2.9g/L; Sigma, G6152), sodium bicarbonate (1.2g/L; Sigma, S5761), penicillin/streptomycin 1% (GIBCO, 15140-122) and Amphotericin B (250ng/mL; Sigma, A2942). After dissection, for all the procedures that required short-term incubations and to optimize steady-state spindle morphology, cortical explants were transferred into 37°C pre-warmed and pre-oxygenated dissection medium supplemented with B27 supplement w/o vitamin A 2% (ThermoFisher, 12587-010), N2 supplement 1% (GIBCO, 17502-048), bFGF (20 ng/ml; Sigma, F0291), EGF (20 ng/ml; Sigma, E9644), horse serum 5% (GIBCO, 16050122) and fetal bovine serum 5% (GIBCO, 1027016) [52]. For all the procedures that required MT visualization, cortical explants were pre-incubated at 37°C for 10 min before any further treatment.

### Human RPE1 cell line culture

Human Retinal Pigmented Epithelial hTERT RPE-1 cells (ATCC Cat# CRL-4000, RRID: CVCL\_4388) were cultured in DMEM/HamF12 medium (GIBCO, 11320-033) supplemented with 10% Foetal Bovine Serum (FBS) (GE Healthcare) and 1% penicillin/streptomycin (GIBCO, 15140-122) on poly-D-lysine (2  $\mu\text{g}/\text{cm}^2$ ; Sigma, P6407) and fibronectin (1  $\mu\text{g}/\text{cm}^2$ ; Sigma, F1141) -coated substrates. Cells were maintained at 37°C in a 5% CO<sub>2</sub> atmosphere. Cells were routinely checked for mycoplasma (PlasmoTest-Mycoplasma Detection Kit, InvivoGen, #rep-pt1) and underwent cell authentication by short tandem repeat analysis (powerplex16 HS kit, Promega #DC2101) processed at the Genomics Platform (Department of the translational research, Curie Institute).

### Primary adherent NSC culture and transfection

To establish primary adherent cultures of NSCs, we have adapted the protocol described in [36]. Cortical explants were dissociated into a single cell suspension by mechanical titration from E16.5 embryonic WT brains (Figure S5A). Cortical cells were plated at a density of 10<sup>4</sup> cells/cm<sup>2</sup> on plastic/glass coverslips pre-coated sequentially for 1h at RT with poly-D-lysine (2  $\mu\text{g}/\text{cm}^2$ ; Sigma, P6407) and fibronectin (1  $\mu\text{g}/\text{cm}^2$ ; Sigma, F1141). Cells were cultured in a medium favoring the propagation of proliferating cells containing DMEM/HamF12 medium (GIBCO, 42400-028), supplemented with glucose (2.9g/L; Sigma, G6152), sodium bicarbonate (1.2g/L; Sigma, S5761), B27 supplement w/o vitamin A 2% (ThermoFisher, 12587-010), FGF (20 ng/ml; Sigma, F0291), EGF (20 ng/ml; Sigma, E9644), penicillin/streptomycin 1% (GIBCO, 15140-122) and Amphotericin B (250ng/ml; Sigma, A2942), at 37°C under 5% CO<sub>2</sub>.

Cortical cell fates and NSC spindle morphology were assessed at day *in vitro* (DIV) 1, DIV3, DIV6 and DIV8 after immunofluorescent staining. In order to have similar cortical cells confluency at the time of fixation, cells were plated at 1.5x10<sup>5</sup> cells/cm<sup>2</sup> (DIV1), 8x10<sup>4</sup> cells/cm<sup>2</sup> (DIV3) and 2.5x10<sup>4</sup> cells/cm<sup>2</sup> (DIV6-DIV8). After one week in culture, more than 80% of the population is composed of Nestin-positive proliferating cells (Neural Stem cells, NSC). Cells were seeded at a density of 10<sup>4</sup> cells/cm<sup>2</sup> for maintenance and passaged with accutase solution (Sigma, A6964) once a week.

## METHOD DETAILS

### Cold-based MT depolymerization and repolymerization assays

MT depolymerization assays were performed by incubating cortical explants at 4°C before fixation at different time points (Figure 2E). For proper analysis of spindle MT decay upon cold treatment, each cortical hemisphere was cut into pieces. For each hemisphere, one piece was fixed before cold treatment to serve as an internal control of preserved bipolar spindle apparatus (steady-state). The other pieces were fixed after 3 min and 7 min of cold treatment for further analysis of MT depolymerization.

MT depolymerization and repolymerization assays were performed by incubating cortical explants at 4°C for 90 min for complete depolymerization of spindle-MTs before allowing those MTs to repolymerize by incubation at 37°C (Figure 2H). Each cortical hemisphere was cut in pieces. One piece was immediately fixed for internal control of steady-state spindles, another piece was fixed after cold treatment to serve as an internal control of complete MT depolymerization. The other piece was fixed after 1 min or 2 min of incubation at 37°C for further analysis of MT repolymerization. The sites of MT repolymerization were investigated after 1 min of repolymerization. For RPE1 cells (Figure S2E), MTs were completely depolymerized for 90 min before repolymerization at 37°C for 45 s and fixation for analysis of sites of MT repolymerization.

### Drug-based assays

Decrease of Eg5 motor protein activity was performed using 1.25  $\mu\text{M}$  Monastrol (Selleckchem, S8439). Chromosomes misalignment and mis-segregation events were promoted using inhibitors of CENP-E motor protein activity (GSK923295, Selleckchem, S7090; 800nM) and Mps1 activity (MPI-0479605, Selleckchem, S7488; 1  $\mu\text{M}$ ). All the drugs were diluted in dimethyl sulfoxide anhydrous (DMSO, Sigma, 276855). Whole cortical explants were incubated for 1h with the drugs at 37°C and washed two times quickly with medium before fixation. Explants incubated with DMSO alone, diluted at equivalent concentrations (V/V), or with medium only were used as negative controls. Chromosome alignment (metaphase) and segregation (anaphase) were assessed in mitotic NSCs after *en face view* analysis of cortical explants (Figures 6 and S6). To evaluate apoptosis (Figures 6E and 6F), explants were incubated for 1h with the drug and washed two times quickly. They were further mounted in a drop of medium surrounded by

10S Voltalef oil (VWR BDH Prolabo, 9002-83-9) and incubated at 37°C in a 5% CO<sub>2</sub> atmosphere for 7h before fixation. They were then sliced manually with a micro-knife before proceeding for immunofluorescent staining to enable visualization of mitotic NSC outcomes along the apico-basal axis.

### In utero injection and electroporation procedures

In utero injection and electroporation procedures were performed as described in [68]. A pool of four different siRNAs for TPX2 was injected through the uterine horns in the lateral ventricles of E15.5 (Figure 4A) or E13.5 (Figure S4D) embryos with a microneedle. Only one hemisphere was injected per embryo and between 4 and 6 embryos per progeny. The concentrations of TPX2 siRNA to be injected in the ventricles were predetermined using *in vitro* adherent NSC cultures. We identified 50nM as a dose partially downregulating TPX2 protein levels without affecting bipolar spindle integrity for the experimental procedures performed in Figures 4, 6, and S6. A dose of 100nM was chosen to fully downregulate TPX2 protein levels for the experimental procedures performed in Figure S4. For each embryo, one brain hemisphere was injected intraventricularly with a solution of fast green 0.1% (Sigma, 68724) in endonuclease free water containing Ctrl (ON-TARGET plus Non-targeting Pool, Dharmacon, D-001810-10-05) or TPX2 siRNA (ON-TARGET plus Mouse TPX2 (72119) siRNA, Dharmacon, #L-055634-01-0005) at 50nM or 100nM. To identify the regions transfected after focal electroporation of the siRNA in the dorsal telencephalon, pEGFP-C1 (Clontech) or a pBLBP-EGFP (kind gift from F. Francis lab, IFM, Paris, France [66];) plasmids were added to the injected solutions at 1μg/μL. Electroporation was performed with a low voltage electric field (5 pulses, 50V, 50ms long, 1 s interval) provided by a BTX-830 electroporator using a pair of tweezerrodes (Sonidel Limited). The electrodes were oriented so that the anode was placed above the dorsal telencephalon of each injected hemisphere. Brains were harvested and fixed 24h (Figures 4, 6, and S6) or 48h (Figure S4) post-electroporation. They were further sectioned with a vibratome and 100 μm-width sections were recovered for lateral views analysis (Figure S4).

### Western blot and FACS sorting of NSCs

Total protein levels in NSCs were evaluated by Western-blot after Nestin-based fluorescence-activated cell sorting (FACS) of E13.5 and E16.5 cortical cells (Figure 3). Dissociated cortical cells were fixed by addition of -20°C precooled EtOH 70% under agitation. They were sequentially incubated with anti-Nestin antibody for 2h at RT (Key Resources Table; 1/100, BD PharMingen, 556309, RRID: AB\_396354) and secondary antibody for 1h at RT (Goat anti-mouse IgG (H+L) Highly Cross-Adsorbed Secondary Antibody, Alexa Fluor 488-conjugated; 1/250, ThermoFisher, A-11029, RRID:AB\_138404) diluted in PBS, BSA 0.5%, saponin 0.1%. Nestin positive cells were sorted using a FACS Aria III systems (BD Biosciences) flow cytometer with an 85 μm nozzle and 45 psi pressure in PBS. Protein extracts were immediately prepared by addition of 4x Laemmli sample buffer (SB) containing Tris/HCl pH6.6 (0.25mM), SDS (8%), β-mercaptoethanol (20%), glycerol (40%) and bromophenol blue (0.1%). For protein denaturation, samples were heated up to 70°C to avoid the generation of protein aggregates. Protein extracts obtained from 1x10<sup>6</sup> Nestin positive cells were loaded per lane, separated in 8% Tris-Glycine gels and transferred by wet electroblotting in Tris 25mM, glycine 192mM, methanol 20% to a 2 μm nitrocellulose membrane for 2h under 100V. Membranes were blocked in PBS, Tween 0.1%, BSA 10% for 30 min at RT followed by 4°C overnight incubation with primary antibodies and 1h RT incubation with HRP-conjugated secondary antibodies. Primary and secondary antibodies used: Rabbit anti-afadin (1/1000, Abcam, ab11337, RRID: AB\_297943), Mouse anti-α-tubulin clone DM1α (1/50000, Sigma T6199, RRID: AB\_477583), Rabbit anti-TPX2 (1/1000, Abnova, PAB11993, RRID: AB\_1716384), Goat anti-Rabbit IgG (H+L) Cross-Adsorbed Secondary Antibody HRP (1/2500, ThermoFisher, G21234, RRID: AB\_2536530), Peroxidase AffiniPure Goat Anti-Mouse IgG (H+L) (1/2500, Jackson ImmunoResearch, 115-035-003, RRID: AB\_10015289).

### Generation of human TPX2 constructs

To obtain full-length (hTPX2 FL) and truncated GFP-hTPX2 versions of the protein (hTPX2 N-TER (aa:1-370); hTPX2 C-TER (aa: 371-747)) the human TPX2 sequence (NCBI Ref Seq: NM\_012112.4; Origene, SC115515) was amplified by PCR (Phusion high-fidelity PCR kit, New England Biolabs, E0553S). XhoI or HindIII restriction sites were added at the 5' end and a KpnI restriction site at the 3' end (all restriction enzymes were purchased from New England Biolabs). The following primers were used for PCR: hTPX2FL forward, 5'-CGCGAAGCTTCAATGTCACAAGTTAAAAGC-3'; hTPX2FL reverse, 5'-CGCGGGTACCTTAGCAGTGGAATCGAGTGG-3'; hTPX2CT forward, 5'-CGCGAAGCTTCAGTACTGCAAACCAAACAC-3'; hTPX2NT forward, 5'-CGCGCTCGAGCAATGTCACAAGTAAAAGC-3'; hTPX2NT reverse, 5'-CGCGGGTACCTTAAGGAGTCTGTGGGTCTC-3'. PCR products were purified according to manufacturer's instructions (QIAquick PCR Purification Kit, ThermoFisher Scientific, 28104), digested and ligated into pCMV-EGFP-C1 (Clontech) using the DNA Ligation Kit (Takara, 6023) and amplified in *E. coli* (strain: DH5α, ThermoFisher Scientific, 18258012).

To generate GFP/hTPX2-\*NLS, a mutagenic PCR was carried out using the GFP-hTPX2FL to change K314, R315, K336 and R337 to alanine by site directed mutagenesis according to the manufacturer's instructions (Q5 Site-Directed Mutagenesis Kit, New England Biolabs, E0554S). The following primers were used for PCR: hTPX2NLS\* forward, 5'-CTTGCACAGCAAGTTGAAGACTTCATGCAGCAACCCCTAACAGATATCATTGTGAGGAGCAAG-3', hTPX2NLS\* reverse, 5'-CTTGCACAGCAAGTTGAAGACTTCCATGCAGCAACCCCTAACAGATATCATTGTGAGGAGCAAG-3'. All constructs were prepared with an endonuclease free maxiprep kit (Endofree Plasmid Maxi Kit, QIAGEN, 12362) for transfection. hTPX2 N-TER, TPX2 C-TER and hTPX2-\*NLS were transfected in E16.5 primary NSCs with the mouse NSC nucleofector kit (Lonza, VPG-1004) according to the manufacturer's instructions. Only cells expressing the GFP-fused versions of the protein were included in the analysis.

### Generation of antibodies

PCR fragments were amplified from mouse *Centrin3* cDNA (NCBI Ref Seq: NM\_007684.3; IMAGE clone ID: 30019209, Thermo Fisher Scientific Biosciences, MMM1013-202805556), mouse *Cep135* cDNA (NCBI Ref Seq: NM\_199032.3; IMAGE clone ID: 6852711, Thermo Fisher Scientific Biosciences, MMM1013-202859840), human *Cep192* cDNA (kind gift from A. Dammermann lab, MPL, Vienna, Austria) and mouse *HSET/Kifc1* cDNA (NCBI Ref Seq: NM\_001195298.1; IMAGE clone ID: 30841951, Thermo Fisher Scientific Biosciences, MMM1013-202780075) using Phusion DNA Polymerase (ThermoFisher Scientific, F530S). The following primers were used: mCentrin3/aa:1-168 forward, 5'-GGGGACAAGTTTGTACAAAAAAGCAGGCTTCATGAGTTTAGCTCTGAGAGGTGAG-3'; mCentrin3/aa:1-168 reverse, 5'-GGGACCACTTTGTACAAGAAAGCTGGGTCTTATATGTCACCAGTCATAATAGC-3'; mCep135/aa:936-1141 forward, 5'-GGGGACAAGTTTGTACAAAAAAGCAGGCTTCAATGCACATCACGCATACGAGTCT-3'; mCep135/aa:936-1141 reverse, 5'-GGGGACCACTTTGTACAAGAAAGCTGGGTCTTATGATCAGGAGT-3'; hCep192/aa:1-210 forward, 5'-GGGACAAGTTTGTACAAAAAAGCAATGGAAGATTTTCGAGGTATAGCA-3'; hCep192/aa:1-210 reverse, 5'-GGGGACCACATTTGTACAAGAAAGCTGGGTCTCAATCTTCCAAGCTTGTGCGTAAGAT-3'; mHSET/aa:1-227 forward, 5'-GGGGACAAGTTTGTACAAAAAAGCAGGTTTCATGGACGTGCAGGCGCAGAGGCCA-3'; mHSET/aa:1-227 reverse, 5'-GGGGACCACTTTGTACAAGAAAGCTGGGTCTTCCCTGGTACCCAG-3'. PCR products were cloned in fusion with the *E.coli malE* gene, which encodes for Maltose Binding Protein (MBP) using the Gateway cloning system (ThermoFisher Scientific, 12535-019). Expression vectors were transformed into competent C41 *E.coli* cells and tested for isopropyl-beta-D-thiogalactopyranoside (IPTG)-mediated recombinant protein expression. Soluble proteins were purified from cell lysates by pre-pure amylose columns containing 4ml amylose resin (New England Biolabs, E8021L) and run on 8% polyacrylamide gels to select the band of appropriate size containing the protein of interest. Rabbit immunizations were performed by Covalab company (Lyon-France). Immune sera were purified sequentially by affinity on MBP protein-bound and antigen-bound columns (Affigel 10, BioRad 153-6052; Affigel 15, BioRad 153-6046). Antibodies were eluted in 0.5 mL glycine 0.1M, pH2.1 buffer, and immediately neutralized in Tris pH8.5. Collected fractions were pooled according to their IgG concentration, evaluated with a Bradford assay. Purified antibodies were stored in glycerol 50% at  $-20^{\circ}\text{C}$  before use.

### Immunofluorescent staining

To better preserve MTs integrity, cortical explants, primary NSC cultures and RPE1 cells were fixed with  $37^{\circ}\text{C}$ -prewarmed paraformaldehyde (PFA) 8% solution directly added to the medium for 15 min at RT, followed by 45 min incubation in PFA 4% at RT. All antibodies were used on PFA-fixed samples; only anti-Eg5 (Figure S3F) and anti-HSET (Figure S3C) antibodies were used on methanol-fixed samples. Methanol fixations were performed for 8 min at  $-20^{\circ}\text{C}$ . An additional step of antigen retrieval (30 min at  $80^{\circ}\text{C}$  in Sodium Citrate 10mM, pH6) was performed for acetylated tubulin (Figure S2A), RCC1 (Figure S5H) and Pax6 (Figure S1C) staining. For cortical explants, a post-fixation permeabilization step with 1% Triton X-100 for 15 min was systematically performed to allow better antibody penetration. Explants were incubated for 1h in blocking solution (PBS, BSA 3%, Triton X-100 0.3%, Sodium azide 0.02%), followed by sequential overnight primary and secondary antibody incubations. Washings were performed with the blocking solution after each incubation. Cortical explants were mounted with the apical surface facing the glass coverslips for further analysis of apically localized mitotic progenitors, as described in [24]. For cells, a solution containing PBS, BSA 2%, Triton X-100 0.1%, Sodium azide 0.02% was used. After a 30 min blocking step, cells were sequentially incubated for 1h at RT with primary and secondary antibodies.

The following primary antibodies were used for analysis: mouse anti-acetylated-tubulin (Sigma, T7451, RRID: AB\_609894); mouse anti- $\alpha$ -tubulin (clone DM1 $\alpha$ , Sigma, T6199, RRID: AB\_477583); mouse anti- $\beta$ -tubulin isotype III (Sigma, T8660, RRID: AB\_477590); rabbit anti-cleaved caspase-3 (Cell Signaling, 9661, RRID: AB\_2341188); rabbit anti-Cdk5rap2 (Bethyl Laboratories, IHC-00063, RRID: AB\_2076863); rabbit anti-CENP-E (kind gift from D. Cleveland lab, LICR, La Jolla, USA [65]); rabbit anti-Centrin-3 (this study); human anti-centromere (Antibodies, 15-235-0001, RRID: AB\_2797146); rabbit anti-Cep135 (this study); rabbit anti-Cep192 (this study); rabbit anti-detyrosinated tubulin (Merck, AB3201, RRID: AB\_303601); rabbit anti-Eg5 (Novus Biologicals, NB500-181, RRID: AB\_10002881); chicken anti-GFP (Abcam, ab13970, RRID: AB\_300798); mouse anti- $\gamma$ -tubulin (clone GTU88, Sigma, T5326, RRID: AB\_532292); rabbit anti-HSET (this study); rabbit anti-NeuN (abcam, ab177487, RRID: AB\_2532109); rabbit anti-NuMA (Novus Biologicals, NB500-174, RRID: AB\_10002562); mouse anti-Pax6 (Millipore, AB2237, RRID: AB\_2270373); rabbit anti-pericentrin (Abcam, ab4448, RRID: AB\_304461); rabbit anti-RCC1 (Proteintech, 22142-1-AP, RRID: AB\_11183045); goat anti-Sox2 (R and D Systems, AF2018, RRID: AB\_355110); rabbit anti-TPX2 (Abnova, PAB11993, RRID: AB\_1716384); rat anti-tyrosinated tubulin (kind gift of C. Janke lab, Curie Institute, Paris, France). The following secondary antibodies from Molecular Probes were used: Goat anti-mouse IgG (H+L) Highly Cross-Adsorbed Alexa Fluor 488-conjugated: A-11029, RRID: AB\_138404; Alexa Fluor 546-conjugated: A-11030, RRID: AB\_144695; Alexa Fluor 647-conjugated: A-21236, RRID: AB\_141725; Goat anti-rabbit IgG (H+L) Highly Cross-Adsorbed Alexa Fluor 488-conjugated: A-11034, RRID: AB\_2576217; Alexa Fluor 546-conjugated: A-11035, RRID: AB\_143051; Alexa Fluor 647-conjugated: A-21245, RRID: AB\_141775; Donkey anti-rabbit IgG (H+L) Highly Cross-Adsorbed Alexa Fluor 568-conjugated: A-10042, RRID: AB\_2534017; Goat anti-chicken IgY (H+L) Highly Cross-Adsorbed Alexa Fluor 488-conjugated: A-11039, RRID: AB\_142924; Goat anti-rat IgG (H+L) Cross-Adsorbed Alexa Fluor 488-conjugated: A-11006, RRID: AB\_141373; Donkey anti-goat IgG (H+L) Alexa Fluor 647-conjugated: A-21447, RRID: AB\_141844; Goat anti-human IgG (H+L) Highly Cross-Adsorbed Alexa Fluor 647-conjugated: A-21445, RRID: AB\_141843. 4',6-diamidino-2-phenylindole (DAPI, ThermoFisher Scientific, D1306, RRID: AB\_2629482) was used to label DNA at a concentration of 3  $\mu\text{g}/\text{ml}$ .

## QUANTIFICATION AND STATISTICAL ANALYSIS

### Evaluation of fluorescence intensity index

Images were acquired on an inverted Leica TCS SP8 confocal microscope with a 63X oil-NA 1.4 Plan Apo immersion objective and hybrid (HyD) detectors at zoom 1 or 2 or on an inverted spinning disk confocal Gattaca/Nikon microscope equipped with a sCMOS camera with a 100X oil-NA 1.4 Plan Apo immersion objective. For comparison purposes, images were acquired with the same settings for each staining combination. Random acquisitions of different cortical regions along the rostro-caudal and the medio-lateral axis were performed for each cortical explant. Images were acquired with a resolution of 1024x1024 pixels along the apico-basal axis with a z-step of 0.2  $\mu\text{m}$ . Only metaphase spindles were included in our analysis based on chromosomes alignment at the center of the bipolar spindle, evaluated by a combination of DNA and centromere staining (not shown). Distribution of  $\alpha$ -tubulin signal intensity (and other spindle associated proteins) was measured along each spindle from pole to pole using the line scan analysis tool of the online Fiji software with a 30 pixels line width and maximum intensity projections of 10 z stacks (2  $\mu\text{m}$ ). The background intensity evaluated from a region of similar area was subtracted in each cell. For each spindle, MT density index or loading of MT associated proteins on spindles were calculated by dividing the minimum fluorescence intensity value at the spindle center over the maximum fluorescence intensity value at the spindle pole (Figure 1C). For distribution of fluorescence signal intensity along the spindles, all the values were normalized to the highest spindle pole value.

### Analysis of spindle architectures

For characterization of spindle architectures (Figures 2A–2D), images were acquired with a N-SIM (Structured Illumination Microscope, Nikon Systems, France), mounted on an inverted Eclipse Ti-E microscope equipped with a motorized XY Stage (Nikon, Japan), equipped with an EMMCD camera (Andor DU-897). Optical sectioning was achieved using a piezo stage (Nano-z series, Mad City Lab, USA). Nikon systems' laser bench was equipped with 488 nm (200mW), 561 nm (100mW) and 640 nm (100mW) lasers coupled to the N-SIM head through a single mode fiber. Correction collar of the Plan Apochromat TIRF SR 100  $\times$  1.49 NA oil immersion objective was optimized to have a symmetrical point spread function. 100 nm size beads were used for calibration before each dataset acquisition (TetraSpeck beads, Life Technologies, T7279). Multiple Point Spread Function was obtained using 0.12  $\mu\text{m}$  z-steps, 15 images per z section (3 angles and 5 phases per angle) and a 3D structured illumination with stripe. 3D-SIM  $\alpha$ -tubulin immunostained spindles were reconstructed manually with the NIS Elements viewer software v4.3.02 (Nikon [67]); by tracing individual MT bundles within each spindle. Centrosomes were identified with pericentrin staining as starting points of each spindle MT bundle. Number and length of MT bundles were extracted from each 3D reconstructed spindle. MT bundle widths were evaluated by measuring the full width at half maximum of the fluorescence intensity profile across each individual MT bundle using the line-scan tool of the online Fiji software. MT bundle width was determined next to the spindle center where individual MT bundle can be best visualized. The same analysis of MT bundle widths was performed after MTs repolymerization (Figure 2J) and TPX2 siRNA (Figure 4F) assays.

For evaluation of astral MT population characteristics (Figures 1F and 1G), the number and length of individual MT bundles nucleated from a spindle pole and directed toward the cell cortex (even if not directly interacting with it) were assessed at the cell equator on images acquired from an *en face* view perspective with the confocal or spinning-disk confocal microscope. Analysis was performed with the measurement tools of the online Fiji software.

### Centrosome organization analysis

For characterization of centrosome organization at mitotic spindle poles (Figures S2G–S2L), images were acquired in cerebral cortical explants with a high resolution OMX microscope (Deltavision). Accumulation of PCM proteins at mitotic centrosomes was evaluated according to [69]. Briefly, line-scan fluorescence intensity profiles were performed across mother centriole PCM rings using the line-scan tool of the online Fiji software. Ring diameter for each marker was evaluated and used as a measure of PCM protein accumulation. Only metaphase centrosomes oriented correctly with the mother PCM ring structure clearly visible were considered for analysis.

### Spindle orientation analysis

For determination of mitotic spindle orientation (Figures 4I–4K), *en face* views of E16.5 cortical explants were immunostained to label DNA (to determine the phase of mitosis), mitotic spindles (to evaluate its morphology) and spindles poles (to depict spindle position). We have restricted our analysis to cells in late metaphase since mitotic spindles stop rotating along the apico-basal axis from metaphase onward [70]. Orthogonal views (xz) of spindles poles were used to determine their position relative to the ventricular surface. Angles were calculated by a tangent function (Figure 4I). The tangent of each  $\alpha$  angle is calculated by dividing the length of the opposite side (o, distance in z between the 2 spindle poles; obtained from orthogonal views) and the length of the adjacent side (a, distance in x between the spindle poles; spindle length). The angle  $\alpha$  was deduced using the Arc Tangent function. Analysis was performed with the measurement tools of the online Fiji software.

### **Quantitative analysis of Western-blot**

Comparative evaluation of protein levels was performed using the “Gel analysis” tool from Fiji online software. Relative density of each band was measured by drawing rectangles of the same size around each band. Density value for each protein of interest was normalized to the density value of the corresponding loading control band.

### **Statistical analysis**

All data plotting and statistical analyses were performed using the GraphPad Prism software (GraphPad software, Inc.). All statistical details for each experiment can be found in the Figures and Figure legends.

For all functional analysis, we performed at least two independent experiments. Results were plotted as mean  $\pm$  SD. All data underwent normality check (Shapiro-Wilk test) and in respect to that, appropriate tests were performed for group comparison (unpaired t test or Mann-Whitney), correlation coefficient assessment between two parameters (Spearman’s test) and evaluation of association between parameters (Chi-square test). Differences were considered statistically significant at values of  $p \leq 0.05$ .

### **DATA AND CODE AVAILABILITY**

No dataset/code associated with the manuscript.